cell activity, receptor expression, or apoptotic events) (*11,12*). Accordingly, nuclear imaging approaches could provide new diagnostic imaging capabilities for detecting vulnerable plaques on the basis of a specific biologic aspect of atherosclerosis progression. Tsimikas et al. reported the use of a ^{99m}Tc-oxidized LDL–specific antibody for atherosclerosis imaging (*28,29*); this agent allowed the detection of atherosclerosis progression and regression. However, oxidized LDL would need to be injected after the use of this agent to reduce a high level of accumulation of the antibody in the blood and liver. Furthermore, LOX-1 may be a more suitable target than oxidized LDL because it is a specific factor in atherosclerosis progression and is expressed during the early period of atherosclerosis. In contrast, nonspecific uptake into atherosclerosis lesions and high permeability of lesions are important concerns (*30,31*). Therefore, we performed a ^{99m}Tc-IgG2a (control probe) study, which showed the specific uptake of ^{99m}Tc-LOX-1-mAb in atherosclerotic plaques.

As representative nuclear imaging probes, ^{18}F-FDG for imaging metabolic activity in macrophages (*19,32*) and ^{99m}Tc-annexin A5 for imaging apoptosis (*33,34*) were recently used for atherosclerotic plaque imaging. Consequently, it was especially important and intriguing to characterize ^{99m}Tc-LOX-1-mAb in the same animal model (WHHLMI rabbits), focusing on the advantages of ^{99m}Tc-LOX-1-mAb. First, the levels of ^{99m}Tc-LOX-1-mAb accumulation were 2.4- and 3.2-fold higher than the levels of ^{18}F-FDG accumulation (DURs, 1.47 ± 0.90 and 0.72 ± 0.37) in the thoracic and abdominal aortic segments in WHHLMI rabbits, respectively (*19*). Additionally, the level of ^{99m}Tc-LOX-1-mAb accumulation was 5.2-fold higher than the level of ^{99m}Tc-annexin A5 accumulation (DUR, 0.64 ± 0.18 [total aorta]) in aortic segments in WHHLMI rabbits (*33*). These results indicated the potential of ^{99m}Tc-LOX-1-mAb for in vivo imaging, as the accumulation level is an essential factor for this purpose.

Second, ^{99m}Tc-LOX-1-mAb accumulated predominantly in atheromatous lesions. The accumulation ratios of ^{99m}Tc-LOX-1-mAb for atheromatous lesions to other lesions (atheromatous/neointimal, atheromatous/fibroatheromatous, and atheromatous/collagen-rich lesion ratios) were higher than those of ^{99m}Tc-annexin A5 (2.7 vs. 1.3, 1.9 vs. 1.3, and 2.4 vs. 1.8, respectively), indicating that ^{99m}Tc-LOX-1-mAb accumulated more selectively in atheromatous lesions. These results suggested the ability of ^{99m}Tc-LOX-1-mAb to selectively detect vulnerable plaques among heterogeneous atherosclerotic lesions.

In noninvasive imaging studies with ^{99m}Tc-LOX-1-mAb, the atherosclerotic abdominal aorta was imaged more clearly in WHHLMI rabbits than in control rabbits, with decreased blood-pool radioactivity in the abdominal aorta (Fig. 7). This result was confirmed in biodistribution studies (Table 1). However, the difference between control and WHHLMI rabbits seemed to be underwhelming when determined from ARG images, for various reasons. First, the spatial resolution of the SPECT images (6.7 mm at full width at half maximum) was lower than that of the ARG images (50 μm). Second, the A/B ratio in WHHLMI rabbits was 0.69 ± 0.33 at 24 h, indicating that the radioactivity detected by noninvasive imaging was attributable to both aorta and blood radioactivity, although this A/B ratio was comparable to that of ^{99m}Tc-annexin A5 (1.0 ± 0.2 at 3 h after injection). Johnson et al. reported the possibility of in vivo imaging of porcine coronary lesions with ^{99m}Tc-annexin A5 (*35*). However, further studies on the acceleration of clearance of radioactivity from the blood pool are necessary. It has been reported that radiopharmaceuticals derived from low-molecular-weight polypeptides or compounds, small recombinant antibody fragments (Fab and scFv), engineered variants (diabodies, triabodies, minibodies, and single-domain antibodies), and pretargeting antibody methods show rapid clearance of radioactivity from the circulation (*36–38*). The technical progression of SPECT devices could also eliminate the high-background problem.

CONCLUSION

We designed and prepared ^{99m}Tc-LOX-1-mAb for the imaging of LOX-1 and characterized the accumulation of ^{99m}Tc-LOX-1-mAb in atherosclerotic lesions in a rabbit model of spontaneous atherosclerosis. We demonstrated that ^{99m}Tc-LOX-1-mAb could evaluate lesion vulnerability more sensitively than other imaging probes. It could be applied in the clinical setting because of the similarity of the histologic characteristics of atherosclerotic plaques in humans and WHHLMI rabbits. ^{99m}Tc-LOX-1-mAb could be useful as a potential imaging probe for predicting lesions prone to spontaneous rupture and monitoring the effects of timely treatment in patients with advanced atherosclerosis.

ACKNOWLEDGMENTS

This work was partly supported by a Grant-in-Aid for General Scientific Research from the Ministry of Education, Culture, Sports, Science and Technology of Japan and from the Japan Society for the Promotion of Science, by a research grant from the New Energy and Industrial Technology Development Organization (NEDO), by a research grant for cardiovascular diseases from the Ministry of Health, Labor and Welfare (16C-8), and by the 21st Century COE Program "Knowledge Information Infrastructure for Genome Science."

REFERENCES

1. Lendon C, Born GV, Davies MJ, Richardson PD. Plaque fissure: the link between atherosclerosis and thrombosis. *Nouv Rev Fr Hematol.* 1992;34:27–29.
2. Ruberg FL, Leopold JA, Loscalzo J. Atherothrombosis: plaque instability and thrombogenesis. *Prog Cardiovasc Dis.* 2002;44:381–394.
3. Kolodgie FD, Virmani R, Burke AP, et al. Pathologic assessment of the vulnerable human coronary plaque. *Heart.* 2004;90:1385–1391.
4. Sawamura T, Kume N, Aoyama T, et al. An endothelial receptor for oxidized low-density lipoprotein. *Nature.* 1997;386:73–77.

5. Kume N, Kita T. Roles of lectin-like oxidized LDL receptor-1 and its soluble forms in atherogenesis. *Curr Opin Lipidol.* 2001;12:419–423.
6. Moriwaki H, Kume N, Kataoka H, et al. Expression of lectin-like oxidized low density lipoprotein receptor-1 in human and murine macrophages: upregulated expression by TNF-alpha. *FEBS Lett.* 1998;440:29–32.
7. Kataoka H, Kume N, Miyamoto S, et al. Oxidized LDL modulates Bax/Bcl-2 through the lectinlike Ox-LDL receptor-1 in vascular smooth muscle cells. *Arterioscler Thromb Vasc Biol.* 2001;21:955–960.
8. Kume N, Kita T. Apoptosis of vascular cells by oxidized LDL: involvement of caspases and LOX-1 and its implication in atherosclerotic plaque rupture. *Circ Res.* 2004;94:269–270.
9. Li D, Liu L, Chen H, et al. LOX-1 mediates oxidized low-density lipoprotein-induced expression of matrix metalloproteinases in human coronary artery endothelial cells. *Circulation.* 2003;107:612–617.
10. Ishino S, Mukai T, Kume N, et al. Lectin-like oxidized LDL receptor-1 (LOX-1) expression is associated with atherosclerotic plaque instability: analysis in hypercholesterolemic rabbits. *Atherosclerosis.* 2007;195:48–56.
11. Jaffer FA, Libby P, Weissleder R. Molecular and cellular imaging of atherosclerosis: emerging applications. *J Am Coll Cardiol.* 2006;47:1328–1338.
12. Davies JR, Rudd JH, Weissberg PL. Molecular and metabolic imaging of atherosclerosis. *J Nucl Med.* 2004;45:1898–1907.
13. Shiomi M, Ito T, Yamada S, et al. Development of an animal model for spontaneous myocardial infarction (WHHLMI rabbit). *Arterioscler Thromb Vasc Biol.* 2003;23:1239–1244.
14. Eto H, Miyata M, Kume N, et al. Expression of lectin-like oxidized LDL receptor-1 in smooth muscle cells after vascular injury. *Biochem Biophys Res Commun.* 2006;341:591–598.
15. Abrams MJ, Juweid M, tenKate CI, et al. Technetium-99m-human polyclonal IgG radiolabeled via the hydrazino nicotinamide derivative for imaging focal sites of infection in rats. *J Nucl Med.* 1990;31:2022–2028.
16. Ono M, Arano Y, Mukai T, et al. Plasma protein binding of ^{99m}Tc-labeled hydrazino nicotinamide derivatized polypeptides and peptides. *Nucl Med Biol.* 2001;28:155–164.
17. Larsen SK, Solomon HF, Caldwell G, et al. [^{99m}Tc]tricine: a useful precursor complex for the radiolabeling of hydrazinonicotinate protein conjugates. *Bioconjug Chem.* 1995;6:635–638.
18. Ishii K, Kita T, Kume N, Nagano Y, Kawai C. Uptake of acetylated LDL by peritoneal macrophages obtained from normal and Watanabe heritable hyperlipidemic rabbits, an animal model for familial hypercholesterolemia. *Biochim Biophys Acta.* 1988;962:387–389.
19. Ogawa M, Ishino S, Mukai T, et al. ^{18}F-FDG accumulation in atherosclerotic plaques: immunohistochemical and PET imaging study. *J Nucl Med.* 2004;45:1245–1250.
20. Stary HC, Chandler AB, Glagov S, et al. A definition of initial, fatty streak, and intermediate lesions of atherosclerosis: a report from the Committee on Vascular Lesions of the Council on Arteriosclerosis, American Heart Association. *Circulation.* 1994;89:2462–2478.
21. Stary HC, Chandler AB, Dinsmore RE, et al. A definition of advanced types of atherosclerotic lesions and a histological classification of atherosclerosis: a report from the Committee on Vascular Lesions of the Council on Arteriosclerosis, American Heart Association. *Circulation.* 1995;92:1355–1374.
22. Kobayashi S, Inoue N, Ohashi Y, et al. Interaction of oxidative stress and inflammatory response in coronary plaque instability: important role of C-reactive protein. *Arterioscler Thromb Vasc Biol.* 2003;23:1398–1404.
23. Shiomi M, Ito T, Hirouchi Y, et al. Stability of atheromatous plaque affected by lesional composition: study of WHHL rabbits treated with statins. *Ann N Y Acad Sci.* 2001;947:419–423.
24. Mann JM, Davies MJ. Vulnerable plaque: relation of characteristics to degree of stenosis in human coronary arteries. *Circulation.* 1996;94:928–931.
25. Falk E, Shah PK, Fuster V. Coronary plaque disruption. *Circulation.* 1995;92: 657–671.
26. Shiomi M, Ito T, Hirouchi Y, et al. Fibromuscular cap composition is important for the stability of established atherosclerotic plaques in mature WHHL rabbits treated with statins. *Atherosclerosis.* 2001;157:75–84.
27. Chen M, Kakutani M, Minami M, et al. Increased expression of lectin-like oxidized low density lipoprotein receptor-1 in initial atherosclerotic lesions of Watanabe heritable hyperlipidemic rabbits. *Arterioscler Thromb Vasc Biol.* 2000;20:1107–1115.
28. Tsimikas S, Palinski W, Halpern SE, Yeung DW, Curtiss LK, Witztum JL. Radiolabeled MDA2, an oxidation-specific, monoclonal antibody, identifies native atherosclerotic lesions in vivo. *J Nucl Cardiol.* 1999;6:41–53.
29. Tsimikas S, Shaw PX. Non-invasive imaging of vulnerable plaques by molecular targeting of oxidized LDL with tagged oxidation-specific antibodies. *J Cell Biochem Suppl.* 2002;39:138–146.
30. Christensen S, Nielsen H. Permeability of arterial endothelium to plasma macromolecules. *Atherosclerosis.* 1977;27:447–463.
31. Smith EB, Staples EM. Distribution of plasma proteins across the human aortic wall: barrier functions of endothelium and internal elastic lamina. *Atherosclerosis.* 1980;37:579–590.
32. Rudd JH, Warburton EA, Fryer TD, et al. Imaging atherosclerotic plaque inflammation with [^{18}F]-fluorodeoxyglucose positron emission tomography. *Circulation.* 2002;105:2708–2711.
33. Ishino S, Kuge Y, Takai N, et al. ^{99m}Tc-annexin A5 for noninvasive characterization of atherosclerotic lesions: imaging and histological studies in myocardial infarction-prone Watanabe heritable hyperlipidemic rabbits. *Eur J Nucl Med Mol Imaging.* 2007;34:889–899.
34. Kietselaer BL, Reutelingsperger CP, Heidendal GA, et al. Noninvasive detection of plaque instability with use of radiolabeled annexin A5 in patients with carotid-artery atherosclerosis. *N Engl J Med.* 2004;350:1472–1473.
35. Johnson LL, Schofield L, Donahay T, et al. ^{99m}Tc-annexin V imaging for in vivo detection of atherosclerotic lesions in porcine coronary arteries. *J Nucl Med.* 2005;46:1186–1193.
36. Behr TM, Becker WS, Bair HJ, et al. Comparison of complete versus fragmented technetium-99m-labeled anti-CEA monoclonal antibodies for immunoscintigraphy in colorectal cancer. *J Nucl Med.* 1995;36:430–441.
37. Sharkey RM, Karacay H, Cardillo TM, et al. Improving the delivery of radionuclides for imaging and therapy of cancer using pretargeting methods. *Clin Cancer Res.* 2005;11:7109–7121.
38. Sakahara H, Saga T. Avidin-biotin system for delivery of diagnostic agents. *Adv Drug Deliv Rev.* 1999;37:89–101.

Available online at www.sciencedirect.com
ScienceDirect
Nuclear Medicine and Biology 36 (2009) 869–876
NUCLEAR MEDICINE — AND — BIOLOGY
www.elsevier.com/locate/nucmedbio

Synthesis and evaluation of a radioiodinated lumiracoxib derivative for the imaging of cyclooxygenase-2 expression

Yuji Kuge[a,b,*], Naoyuki Obokata[a], Hiroyuki Kimura[a], Yumiko Katada[a], Takashi Temma[a], Yukihiko Sugimoto[c], Kazuki Aita[a,d], Koh-ichi Seki[d], Nagara Tamaki[e], Hideo Saji[a]

[a]*Department of Patho-Functional Bioanalysis, Graduate School of Pharmaceutical Sciences, Kyoto University, Kyoto 606-8501, Japan*
[b]*Department of Tracer Kinetics and Bioanalysis, Graduate School of Medicine, Hokkaido University, Sapporo 060-8638, Japan*
[c]*Department of Physiological Chemistry, Graduate School of Pharmaceutical Sciences, Kyoto University, Kyoto 606-8501, Japan*
[d]*Central Institute of Isotope Science, Hokkaido University, Sapporo 060-8638, Japan*
[e]*Department of Nuclear Medicine, Graduate School of Medicine, Hokkaido University, Sapporo 060-8638, Japan*

Received 18 February 2009; received in revised form 14 July 2009; accepted 26 July 2009

Abstract

Introduction: Despite extensive attempts to develop cyclooxygenase (COX)-2 imaging radiotracers, no suitable positron emission tomography (PET)/single photon emission computed tomography (SPECT) tracers are currently available for in vivo imaging of COX-2 expression. The aims of this study were to synthesize and evaluate a radioiodinated derivative of lumiracoxib, 2-[(2-fluoro-6-iodophenyl)-amino]-5-methylphenylacetic acid (FIMA), which is structurally distinct from other drugs in the class and has weakly acidic properties, as a SPECT tracer for imaging COX-2 expression.

Methods: The COX inhibitory potency was assessed by measuring COX-catalyzed oxidation with hydrogen peroxide. Cell uptake characteristics of ^{125}I-FIMA were assessed in control and linterfero/interferon-γ-stimulated macrophages. The biodistribution of ^{125}I-FIMA was determined by the ex vivo tissue counting method in rats.

Results: The COX-2 inhibitory potency of FIMA (IC_{50}=2.46 μM) was higher than that of indomethacin (IC_{50}=20.9 μM) and was comparable to lumiracoxib (IC_{50}=0.77 μM) and diclofenac (IC_{50}=0.98 μM). The IC_{50} ratio (COX-1/COX-2=182) indicated FIMA has a high isoform selectivity for COX-2. ^{125}I-FIMA showed a significantly higher accumulation in COX-2 induced macrophages than in control macrophages, which decreased with nonradioactive FIMA in a concentration dependent manner. The biodistribution study showed rapid clearance of ^{125}I-FIMA from the blood and most organs including the liver and kidneys. No significant in vivo deiodination was observed with radioiodinated FIMA.

Conclusions: FIMA showed high inhibitory potency and selectivity for COX-2. Radioiodinated FIMA showed specific accumulation into COX-2 induced macrophages, no significant in vivo deiodination and rapid blood clearance. Radioiodinated FIMA deserves further investigation as a SPECT radiopharmaceutical for imaging COX-2 expression.

Keywords: Cyclooxygenase-2; Inhibitor; Radioiodination; SPECT; Radiopharmaceutical

1. Introduction

Cyclooxygenases (COXs) are the key rate-limiting enzymes in the conversion of arachidonic acid to prostaglandins and thromboxanes. To date, at least two distinct isoforms of the COXs, a constitutive isoform (COX-1) and an inducible isoform (COX-2), and several of their variants have been discovered [1]. COX-2 plays important roles in response to inflammatory stimuli and has been implicated in a number of pathological processes including many human cancers, atherosclerosis and cerebral and cardiac ischemia [2–5]. We have also reported the association of COX-2 expression with cerebral ischemia and

* Corresponding author. Department of Tracer Kinetics and Bioanalysis, Graduate School of Medicine, Hokkaido University, Sapporo 060-8638, Japan. Tel.: +81 11 706 5085, fax: +81 11 706 7155.
E-mail address: kuge@med.hokudai.ac.jp (Y. Kuge).

0969-8051/$ – see front matter © 2009 Elsevier Inc. All rights reserved.
doi:10.1016/j.nucmedbio.2009.07.006

atherosclerosis using rodent and primate models of these diseases [6–11].

Accordingly, noninvasive imaging of COX-2 expression would be useful for early diagnosis and for monitoring the progression and treatment efficacy for such diseases [12,13]. In this regard, several COX-2 inhibitors including ^{18}F-SC58125, ^{18}F-desbromo-DuP-697, ^{11}C-celecoxib, ^{11}C-rofecoxib and ^{123}I-celecoxib analogues have been radiolabeled and evaluated as potential tracers for positron emission tomography (PET) and single photon emission tomography (SPECT) [14–24] (Fig. 1). We have contributed to this area with the synthesis and preliminary evaluation of radioiodinated celecoxib analogues [22]. Results, however, have not been entirely consistent between laboratories due to what is generally ascribed to the relatively high nonspecific binding of these compounds [23–26]. The effect of this high nonspecific binding on results appears to be largely dependent on experimental conditions and could cause inconsistent findings. Thus, no appropriate PET/SPECT tracers are currently available for in vivo imaging of COX-2 expression [23–25]. In the search for suitable PET/SPECT tracers for COX-2 imaging, attempts have recently been made to radiolabel new generation COX-2 inhibitors which have greater inhibitory potencies and selectivities for COX-2 [25–27]. However, to date, the radiolabeled COX-2 inhibitors evaluated as PET/SPECT tracers exclusively possess the same basic skeleton, a cyclic core with two vicinal aryl rings.

Another new generation COX-2 selective inhibitor, lumiracoxib, is structurally distinct from other drugs in the class and has weakly acidic properties [28–31]. The K_i and IC_{50} values of lumiracoxib for COX-2 are better than or comparable to those of other COX-2 inhibitors including celecoxib [28]. Lumiracoxib is distributed and retained in inflamed tissues while being rapidly cleared from plasma with a short elimination half-life [30–32]. Thus, we selected lumiracoxib as a lead compound for a potential COX-2 imaging tracer. In this study, a radioiodinated derivative of lumiracoxib, 2-[(2-Fluoro-6-iodophenyl)-amino]-5-methylphenylacetic acid (FIMA) was synthesized and its potential as an imaging tracer was assessed in both in vitro and in vivo experiments.

2. Materials and methods

2.1. General

Sodium ^{125}I-iodide (642.8 GBq/mg) was purchased from Perkin Elmer Life and Analytical Sciences (Boston, MA, USA). All chemicals used were of reagent grade.

Proton and carbon nuclear magnetic resonance spectra were recorded on a JMM-ECA500KP spectrometer (JEOL, Tokyo, Japan). The chemical shifts are reported in parts per million (ppm) downfield from an internal tetramethylsilane standard. Mass spectra were recorded with a JMS-HX/HX110A, JMS-SX102AQQ or JMS-GC-mate spectrometer (JEOL).

2.2. Synthesis

2.2.1. Synthesis of FIMA (5)

FIMA was synthesized according to the procedure outlined in Fig. 2.

Compound **2** was synthesized in three steps according to the method reported by Acemoglu et al. [33]. Briefly, *p*-iodotoluene (189 μl, 1.4 mmol) was coupled with 2-bromo-6-fluoroaniline (158 μl, 1.4 mmol), utilizing the Pd(0) catalyzed Buchwald–Hartwig reaction, to give 1 as a colorless oil with a yield of 27%. Compound **1** (771.5 mg, 2.75 mmol) was acylated with bromoacetyl bromide (288 μl, 3.30 mmol) and then subjected to a Friedel-Crafts alkylation to obtain **2** as a yellowish powder with a yield of 39% (Mp, 118–120°C).

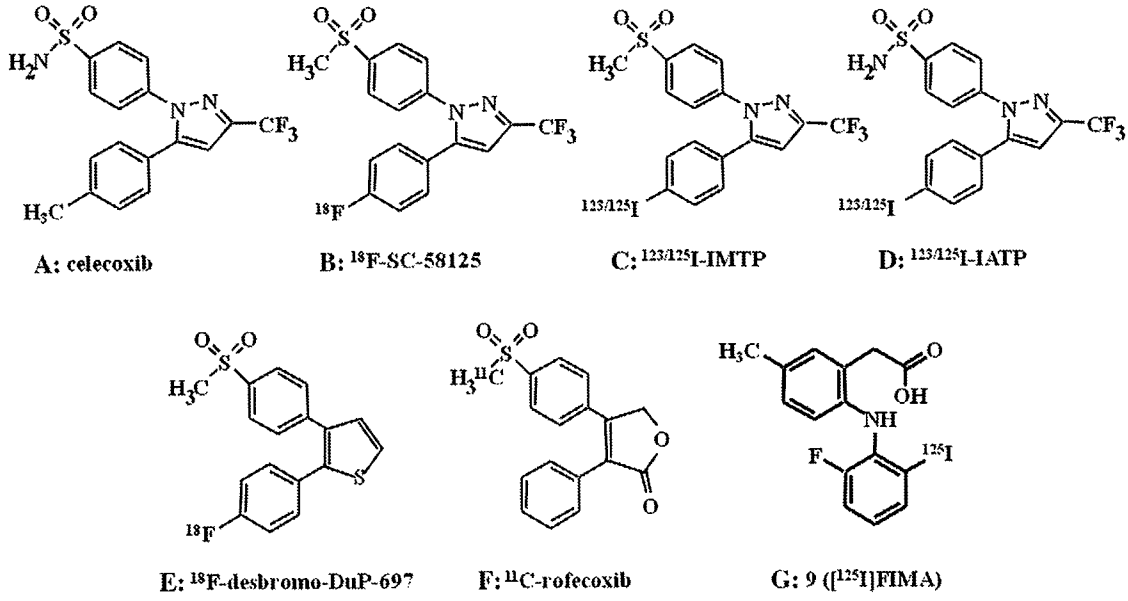

Fig. 1. Chemical structures of radiolabeled COX-2 inhibitors.

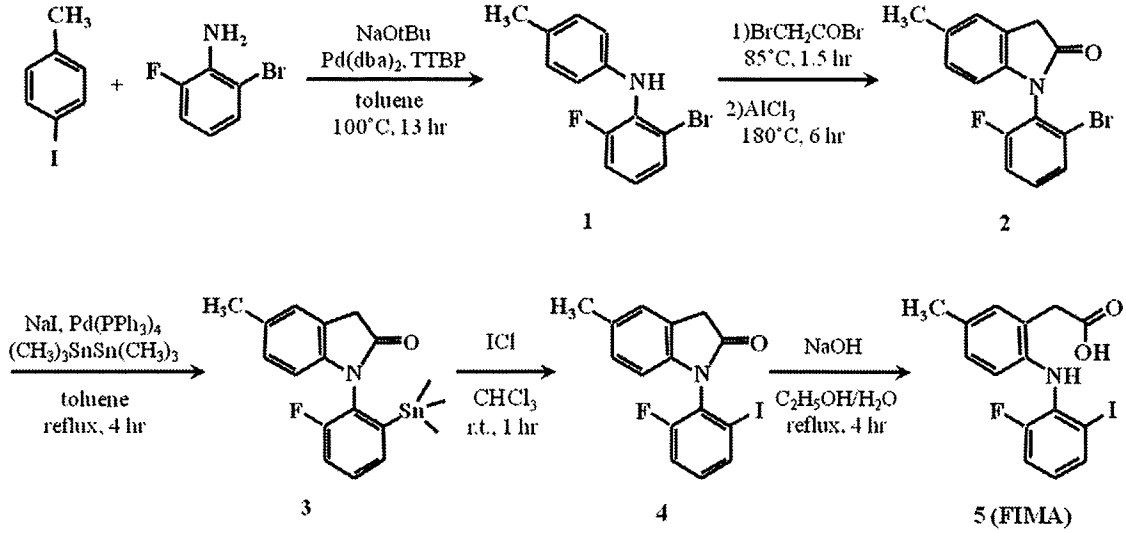

Fig. 2. Synthesis of FIMA (compound 5). Compound **1**, *N*-(2-Bromo-6-fluorophenyl)-4-methylaniline; Compound **2**, *N*-(2′-Bromo-6′-fluorophenyl)-5-methyloxindole; Compound **3**, *N*-(2′-fluoro-6′-trimethylstannanylphenyl)-5-methyl-oxindole; Compound **4**, *N*-(2′-Fluoro-6′-iodophenyl)-5-methyloxindole; Compound **5**, FIMA.

To a solution of **2** (140.7 mg, 0.44 mmol) in 10 ml of toluene at room temperature under a nitrogen atmosphere, NaI (197.6 mg, 1.32 mmol) was added. After stirring at 85°C for 30 min, tetrakis(triphenylphosphine)-palladium(0) (127 mg, 0.11 mmol) and hexamethylditin(IV) (182.3 μl, 0.88 mmol) were added and the solution was refluxed for 4 h. The reaction mixture was filtered and evaporated in vacuo. The residue was purified by silica gel column chromatography (*n*-hexane/ethyl acetate, 6/1) to give **3** as a yellowish powder with a yield of 38% (Mp, 124-127°C).

To a solution of **3** (96.9 mg, 0.24 mmol) in 1 ml of chloroform under an argon atmosphere, iodine monochloride (46.7 mg, 0.29 mmol) in 1 ml of chloroform was added, and the mixture was stirred at room temperature for 1 h. The reaction mixture was washed with saturated sodium thiosulfate and extracted with chloroform. The organic layer was dried over Na_2SO_4, filtered and concentrated in vacuo. The residue was purified by silica gel column chromatography (*n*-hexane/ethyl acetate, 4/1) to give **4** as a pinkish powder with a yield of 85% (Mp, 149-153°C).

To a solution of **4** (61.4 mg, 0.17 mmol) in EtOH/purified water (750 μl/60 μl) under reflux at 95°C, 30% (w/w) NaOH (60 μl) was added dropwise, and the reaction was further refluxed for 4 h. The reaction mixture was allowed to cool to room temperature and then was acidified with 12 N HCl to pH 3.0. Purified water was added to the mixture to give a

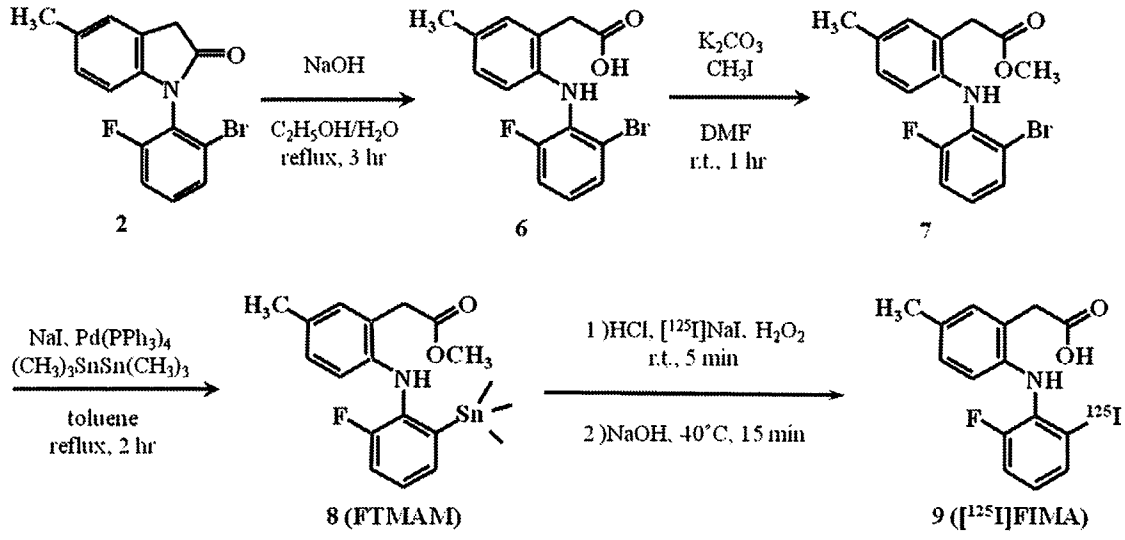

Fig. 3. Synthesis of FTMAM (Compound **8**) and ^{125}I-FIMA (compound **9**). Compound 2, *N*-(2′-Bromo-6′-fluorophenyl)-5-methyloxindole; Compound **6**, 2-[(2-bromo-6-fluorophenyl)amino]-5-methylphenylacetic acid; Compound **7**, 2-[(2-bromo-6-fluorophenyl)amino]-5-methylpheny-lacetic acid methyl ester; Compound **8**, FTMAM; Compound **9**, 2-[(2-fluoro-6-[^{125}I]iodophenyl)amino]-5-methylphenyl-acetic acid (^{125}I-FIMA).

precipitate. The precipitate was filtered, washed with purified water and dried to give **5** as a yellowish ocher powder with a yield of 92% (Mp, 149-152°C). ^{1}H NMR (500 MHz, $CDCl_3$) δ, 7.60 (dt, *J*=8.0, 1.2 Hz, 1H), 7.03-7.07 (m, 2H), 6.96 (dd, *J*=8.0, 1.6 Hz, 1H), 6.74 (td, *J*=8.1, 5.2 Hz, 1H), 6.59 (dd, *J*=8.2, 2.4 Hz, 1H), 6.30 (br s, 1H), 3.79 (s, 2H), 2.28 (s, 3H). HRFABMS: Calcd for $C_{15}H_{13}FINO_2$ $(M+H)^+$, *m/z* 384.9975, found 384.9971.

2.2.2. Synthesis of 2-[(2-fluoro-6-trimethylstannanylphenyl) amino]-5-methylphenylacetic acid methyl ester (8)

2-[(2-Fluoro-6-trimethylstannanylphenyl)amino]-5-methylphenylacetic acid methyl ester (FTMAM) was synthesized according to the procedure outlined in Fig. 3. Compound **6** was synthesized from **2** with a yield of 98% (Mp, 131-134°C) using the same procedure as for FIMA from **4**. To a solution of **6** (142 mg, 0.42 mmol) in 4 ml of Dimethylformamide at room temperature under a nitrogen atmosphere, K_2CO_3 (87.1 mg, 0.63 mmol) was added, and the mixture was stirred for 10 min. Methyl iodide (39.3 μl, 0.63 mmol) was added to the reaction mixture, and the mixture was further stirred at room temperature for 1 h. After the completion of the reaction, ice chilled, purified water was added and the mixture was extracted with ethyl acetate. The organic layer was dried over Na_2SO_4, filtered and concentrated in vacuo. The crude product was purified by silica gel column chromatography (*n*-hexane/ethyl acetate, 4/1) to give **7** as a colorless solid with a yield of 95% (Mp, 55–60°C). FTMAM (**8**) was synthesized from **7** in a similar procedure as for **3** from **2**, except that the crude product was purified by preparative TLC (*n*-hexane/ethyl acetate, 4/1) to give FTMAM (**8**) as a colorless oil with a yield of 30%. Compound **6**: 1H NMR (400 MHz, DMSO-d_6) δ, 7.50 (dt, *J*=8.2, 1.2 Hz, 1H), 7.27 (ddd, *J*=10.9, 8.3, 1.2 Hz, 1H), 7.01-7.07 (m, 3H), 6.90 (dd, *J*=8.0, 1.2 Hz, 1H), 6.39 (dd, *J*=8.0, 2.6 Hz, 1H), 3.63 (s, 2H), 2.21 (s, 3H). HREIMS: Calcd for $C_{15}H_{13}BrFNO_2$ $(M+H)^+$, *m/z* 337.0113, found 337.0120. Compound **7**: 1H NMR (500 MHz, $CDCl_3$) δ, 7.37 (d, *J*=8.2 Hz, 1H), 7.01-7.04 (m, 2H), 6.95 (d, *J*=8.0 Hz, 1H), 6.85 (ddd, *J*=8.2, 8.0, 5.4 Hz, 1H), 6.63-6.65 (m, 2H), 3.76 (s, 2H), 3.74 (s, 3H), 2.28 (s, 3H). HREIMS: Calcd for $C_{16}H_{15}BrFNO_2$ $(M+H)^+$, *m/z* 351.0270, found 351.0264. Compound **8** (FTMAM): ^{1}H NMR (500 MHz, acetone-d_6) δ, 7.32 (dd, *J*=7.2, 1.4 Hz, 1H), 7.25 (ddd, *J*=8.1, 7.2, 4.5 Hz, 1H), 7.17 (ddd, *J*=10.6, 8.1, 1.4 Hz, 1H), 7.02 (s, 1H), 6.86 (d, *J*=8.2 Hz, 1H), 6.59 (br s, 1H), 6.28 (d, *J*=8.2 Hz, 1H), 3.76 (s, 2H), 3.70 (s, 3H), 2.21 (s, 3H), 0.11 (s, 9H). HREIMS: Calcd for $C_{19}H_{24}FNO_2Sn$ $(M+H)^+$, *m/z* 437.0813, found 437.0808.

2.2.3. Synthesis of lumiracoxib

Lumiracoxib, synthesized according to the method of Acemoglu et al. [33] using *p*-iodotoluene and 2-chloro-6-fluoroaniline as starting materials, was obtained as a brownish powder. ^{1}H NMR (400 MHz, DMSO-d6) δ, 12.65 (br s, 1H), 7.35 (dd, *J*=8.3, 1.2 Hz, 1H), 7.23 (ddd, *J*=9.5, 8.3, 1.2 Hz, 1H), 7.06-7.11 (m, 2H), 7.01 (br s, 1H), 6.91 (br d, *J*=8.0 Hz, 1H), 6.42 (dd, *J*=8.3, 2.9 Hz, 1H), 3.65 (s, 2H), 2.21 (s, 3H). HRFABMS: Calcd for $C_{15}H_{13}ClFNO_2$ $(M+H)^+$, *m/z* 293.0619, found 293.0622.

2.3. Radiolabeling

Electrophilic iododestannylation of FTMAM (8) with sodium ^{125}I-iodine and H_2O_2 generated ^{125}I-FIMA as outlined in Fig. 3. Briefly, to a solution of FTMAM in 10 μl of EtOH (1 mg/ml) in a vial, 1 N HCl (15 μl), 12.3 MBq of sodium ^{125}I-iodine in 0.2 N NaOH (7.5 μl, carrier-free) and 30% H_2O_2 (2 μl) were added, and the mixture was stirred at room temperature for 5 min. After cooling with ice, saturated $NaHSO_3$ was added to the reaction mixture to terminate the reaction. The reaction mixture was basified with 1 N NaOH to pH 9.0 at room temperature and then was stirred at 40 °C for 15 min. The solution was applied to a reverse-phase high-performance liquid chromatography (HPLC) column (Cosmosil 5C18-AR-II 4.6 mm injected does × 150 mm, Nacalai Tesque, Kyoto, Japan) and eluted at a flow rate of 1.0 ml/min with 20 mM phosphate buffer (pH 2.5): MeOH=30: 70 for the purification of ^{125}I-FIMA (R_t=17 min). The radiochemical purity of the labeled compound was determined by analytical HPLC using the same conditions as described above. The radiochemical purity and specific activity were determined to be greater than 95% (*n*=3) and 47–72 GBq/μmol (*n*=3), respectively.

2.4. COX inhibitory potency

Peroxidase inhibitory activity of FIMA was assessed by measuring the COX-catalyzed oxidation of *N,N,N′,N′*-tetramethyl-*p*-phenylenediamine (TMPD) by hydrogen peroxide using a commercially available kit (Colorimetric COX Inhibitor Screening Assay Kit, Cayman Chemical, Ann Arbor, MI, USA) as previously described [22]. Briefly, 10 μl of ovine COX-1 or COX-2 solution was added to a 96-well plate with 150 μl of 0.1 mol/L Tris buffer at pH 8.0, 10 μl of heme solution in DMSO, and 10 μl of the test compound (final concentration: 10^{-3}–10^{-9} mol/L). After a 5-min incubation at 25°C, 20 μl of TMPD and 20 μl of 1.1 mM arachidonic acid were added to the mixture. The oxidation of TMPD was monitored by measuring the absorbance of the mixture with a plate reader at 600 nm. Lumiracoxib, diclofenac and indomethacin were used as reference compounds.

2.5. Distribution coefficients

^{125}I-FIMA in a mixture of 2 ml of octanol and 2 ml of 0.1 M phosphate buffer (pH 7.4) was shaken three times for 1 min and then left for 20 min. This procedure was repeated three times, and then the layers were separated by centrifugation. An aliquot of each layer was counted in an auto well gamma counter (Cobra II Auto-Gamma, Packard, Tokyo, Japan). The mean of 3–4 independent octanol-buffer distribution coefficient measurements was expressed as the

$logD_{7.4}$. Radioiodinated analogues of celecoxib, 5-(4-[^{125}I] iodophenyl)-1-[4-(methylsulfonyl)phenyl]-3-trifluoromethyl-1*H*-pyrazole (^{125}I-IMTP) and 5-(4-[^{125}I]iodophenyl)-1-[4-(aminosulfonyl)phenyl]-3-trifluoromethyl-1*H*-pyrazole (^{125}I-IATP) [22] were used as reference compounds.

2.6. In vitro cell uptake study

Since the conventional murine macrophage-like cell line J774.1 is composed of a heterogeneous mixture of cells, JA-4 cells were subcloned from J774.1 cells to obtain a homogeneous cell population. The culturing of JA-4 cells was performed as described previously [34]. In brief, the cells were maintained and cultured in 10 ml of Ham's F-12 medium (Flow Laboratories, McLean, VA, USA), supplemented with 10% heat-inactivated fetal bovine serum (GIBCO, Grand Island, NY, USA), 50 U/ml of penicillin and 50 mg/ml of streptomycin (Flow Laboratories) in a 100-mm plastic dish (Falcon #1001; Becton Dickinson, Lincoln Park, NJ, USA) at 37°C in a CO_2 incubator (5% CO_2-95% humidified air). In order to induce COX-2, aliquots of the cell suspension were placed into 12-well plates and stimulated with linterfero (LPS, 10 μg/ml) and interferon-γ (IFN-γ, 50 U/ml) for 18 h at 37°C in a humidified atmosphere containing 5% CO_2 and 20% O_2. The stimulated and control cells were washed twice with HEPES-buffered Krebs solution (131 mM NaCl, 5.5 mM KCl, 1 mM $MgCl_2$, 2.5 mM $CaCl_2$, 25 mM $NaHCO_3$, 1 mM NaH_2PO_4, 5.5 mM D-glucose, 20 mM HEPES, pH 7.4). After incubation in HEPES buffer at 37°C for 10 min, ^{125}I-FIMA (37 kBq/ml) was added with nonradioactive FIMA (none and 10^{-9} to 10^{-5} M in final concentration), and the cells were incubated at 37°C for 60 min and then were washed twice with ice cold phosphate-buffered saline. The cells were lysed with 1% (w/v) sodium dodecyl sulfate and 10 mM sodium tetraborate decahydrate, collected and counted in an auto well gamma counter (Cobra II Auto-Gamma, Packard, Tokyo, Japan). The protein content was determined using a BCA protein assay kit (Thermo Fisher Scientific, Waltham, MA, USA). The uptake levels of ^{125}I-FIMA are expressed as the percentage of incubated dose per mg protein (% dose/mg protein).

2.7. Western blotting

COX-2 expression levels in the stimulated and control macrophage-like cells (JA-4) were examined by Western blotting. Each cell lysate, prepared from the stimulated and control cells, was mixed with a sample buffer (1% sodium dodecyl sulfate, 10% glycerol, 62.5 mM Tris-HCl (pH 6.8), 0.01% bromo phenol blue, 5% 2-mercaptoethanol) and was subjected to electrophoresis on sodium dodecyl sulfate, 5–20% polyacrylamide gel, followed by transfer to a polyvinylidene difluoride membrane. After blocking with Blocking One (03953-95, Nacalai Tesque, Kyoto, Japan), membranes were incubated with the anti-COX-2 antibody (rabbit polyclonal antibody to murine COX-2 amino acids 570-598, Cayman Chemical), followed by horseradish peroxidase-conjugated swine anti-rabbit immunoglobulin antibody. Bands were visualized by the ECL plus Western Blotting Detection System (RPN2132, GE Healthcare UK. Buckinghamshire, England) using a Luminocapture instrument (BIO-RAD Laboratories, Hercules, CA). Immunoblotting for β-actin was used as a protein loading control.

2.8. Animal experiments

Animal studies were conducted in accordance with institutional guidelines, and experimental procedures were approved by the Kyoto University Animal Care Committee.

Biodistribution studies of ^{125}I-FIMA were performed in male Sprague–Dawley rats (280–310 g). ^{125}I-FIMA (74 kBq/rat) was administered to rats under chloral hydrate anesthesia by tail vein injection. At 10, 30, 60 and 180 min after administration, rats were sacrificed by exsanguination under chloral hydrate anesthesia. Blood and organs were excised and weighed, and radioactivity was measured with an auto well gamma counter (ARC2000, Aloka, Tokyo, Japan). Radioactivity levels in the tissues are expressed as the percentage of injected dose per organ (% ID) and/or the percentage of injected dose per gram of tissue (% ID/g).

3. Results

3.1. Synthesis and radiolabeling

FIMA, FTMAM and lumiracoxib were obtained with overall yields of 7.2%, 6.4% and 19.4%, respectively, from the corresponding starting materials. The radiosynthesis of ^{125}I-FIMA was achieved with an electrophilic iododestannylation reaction. ^{125}I-FIMA was obtained with no carrier being added following separation from the precursor (FTMAM) using reverse phase HPLC with a radiochemical yield of 36–51% (n=3). The radiochemical purity and specific activity were determined to be greater than 95% (n=3) and 47–72 GBq/μmol (n=3), respectively.

3.2. COX inhibitory potency

FIMA inhibited COX-2 in a concentration dependent manner, while showing no inhibitory potency for COX-1 in concentrations up to 10^{-4} M. Table 1 summarizes the IC_{50} values of the test compounds. The IC_{50} value of FIMA was 2.46 μM for COX-2 and 446 μM for COX-1. The COX-2 inhibitory potency of FIMA was higher than that of indomethacin (IC_{50}=20.9 μM) and was comparable to the potencies of lumiracoxib (IC_{50}=0.77 μM) and diclofenac (IC_{50}=0.98 μM). The IC_{50} ratio (COX-1/COX-2) for FIMA was 182 which is comparable to that of lumiracoxib.

3.3. Distribution coefficients

The distribution coefficient ($logD_{7.4}$) of ^{125}I-FIMA was 1.84±0.01 (n=4) and was less than those of the two radioligands, ^{125}I-IMTP ($logD_{7.4}$=3.09±0.11, n=3) and

Table 1
COX inhibitory potency and selectivity of FIMA and reference compounds

Compounds	IC_{50} (μM)		IC_{50} ratio (COX-1/COX-2)
	COX-1	COX-2	
FIMA	446±317	2.46±0.78	182
Lumiracoxib	164±75	0.77±0.21	214
Diclofenac	0.12±0.08	0.98±0.26	0.12
Indomethacin	0.19±0.13	20.9±10.4	0.009

Mean±S.D. for three to four independent experiments.

^{125}I-IATP ($logD_{7.4}$=2.97±0.01, n=4) which were used as reference compounds.

3.4. In vitro cell uptake study

Cell uptake characteristics of ^{125}I-FIMA were assessed in control and LPS/IFN-γ-stimulated macrophages (Fig. 4). The accumulation level of ^{125}I-FIMA in LPS/IFN-γ-stimulated macrophages was significantly higher than that in control macrophages under conditions without nonradioactive FIMA. The accumulation level of ^{125}I-FIMA in LPS/IFN-γ-stimulated macrophages decreased with the addition of nonradioactive FIMA in a concentration dependent manner, while in control macrophages, the accumulation level was unaffected by added nonradioactive FIMA.

Western blot analysis confirmed a significant COX-2 expression in LPS/IFN-γ-stimulated macrophages while no obvious COX-2 expression was observed in control macrophages (Fig. 4B).

3.5. Biodistribution

The biodistribution of ^{125}I-FIMA in normal rats is shown in Table 2. Radioactivity in the blood decreased rapidly and the level was 0.08±0.02% ID/g at 180 min after tracer administration. At 10 min after the injection, high levels of radioactivity were found in the liver and kidneys but

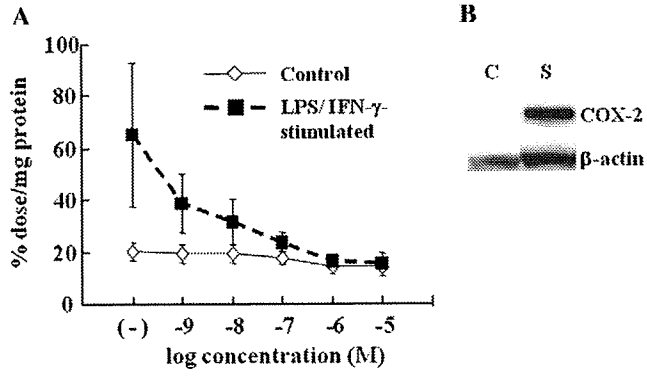

Fig. 4. ^{125}I-FIMA accumulation and COX-2 expression in LPS/IFN-γ-stimulated and control macrophages. (A) ^{125}I-FIMA and nonradioactive FIMA (0, 10^{-9}–10^{-5} M) were incubated with macrophages for 60 min. Mean±S.D. for four experiments. (B) Western blot analysis of COX-2 expression. C, control; S, LPS/IFN-γ-stimulated macrophages.

Table 2
Biodistribution of ^{125}I-FIMA in normal rats

		Time after injection (min)			
		10	30	60	180
Blood	% ID/g	0.55±0.18	0.24±0.02	0.18±0.01	0.08±0.02
Plasma	% ID/g	1.28±0.40	0.57±0.05	0.44±0.05	0.19±0.05
Muscle	% ID/g	0.09±0.03	0.04±0.01	0.03±0.01	0.02±0.00
Heart	% ID/g	0.28±0.10	0.12±0.01	0.08±0.01	0.03±0.01
	% ID	0.24±0.08	0.11±0.01	0.08±0.02	0.03±0.01
Lung	% ID/g	0.36±0.10	0.27±0.19	0.14±0.01	0.07±0.01
	% ID	0.43±0.13	0.38±0.26	0.17±0.02	0.07±0.02
Liver	% ID/g	2.93±1.10	1.04±0.14	0.67±0.05	0.28±0.04
	% ID	25.5±10.4	9.90±0.99	5.88±0.61	2.48±0.35
Kidneys	% ID/g	0.95±0.39	0.81±0.13	0.63±0.09	0.33±0.10
	% ID	2.18±0.87	1.90±0.19	1.49±0.25	0.76±0.23
Pancreas	% ID/g	0.18±0.05	0.10±0.02	0.07±0.01	0.04±0.01
	% ID	0.11±0.06	0.05±0.01	0.03±0.00	0.02±0.01
Spleen	% ID/g	0.14±0.04	0.10±0.05	0.05±0.01	0.03±0.01
	% ID	0.07±0.02	0.05±0.02	0.03±0.00	0.01±0.00
Stomach	% ID/g	0.47±0.19	0.86±0.46	1.28±1.00	0.50±0.27
	% ID	1.00±0.40	1.77±0.97	2.64±1.92	0.95±0.50
Intestine	% ID/g	0.33±0.19	0.46±0.16	0.83±0.14	1.70±0.32
	% ID	4.95±3.08	7.30±3.34	12.16±2.56	22.46±2.39
Brain	% ID/g	0.04±0.02	0.02±0.00	0.02±0.00	0.01±0.00
	% ID	0.08±0.03	0.04±0.00	0.03±0.00	0.01±0.00
Thyroids	% ID/g	1.15±1.06	0.57±0.08	2.28±2.14	6.60±3.58
	% ID	0.01±0.00	0.01±0.00	0.01±0.00	0.03±0.02

Mean±S.D. for five animals.

decreased with time. The radioactivity level in the intestine gradually increased with time and reached 1.70±0.32% ID/g at 180 min. ^{125}I-FIMA showed no significant accumulation in the stomach and thyroid, and the maximum accumulation doses in these tissues were 2.64% ID (60 min) and 0.03% ID (180 min), respectively. Significant levels of radioactivity were not found in the brains of rats.

4. Discussion

In this study, we synthesized a radioiodinated lumiracoxib derivative, 2-[(2-Fluoro-6-[^{125}I]iodophenyl)amino]-5-methylphenyl-acetic acid (^{125}I-FIMA). The potential of radioiodinated FIMA for imaging COX-2 expression was evaluated by in vitro and in vivo experiments. The major findings in this study can be summarized as follows: (1) FIMA had a high inhibitory potency and isoform selectivity for COX-2. (2) ^{125}I-FIMA showed a significantly higher accumulation in COX-2 induced macrophages than in control macrophages, which decreased with the addition of nonradioactive FIMA in a concentration dependent manner. (3) The biodistribution study in normal rats showed rapid clearance of ^{125}I-FIMA from the blood and most organs without significant in vivo deiodination of ^{125}I-FIMA. These results indicate radiolabeled lumiracoxib derivatives have the potential to be PET/SPECT tracers of COX-2 expression. Affinity and specificity including isoform selectivity for COX-2 are indispensable prerequisites of PET/SPECT tracers for imaging the enzyme.

The COX-2 inhibitory potency and isoform selectivity of FIMA were comparable to those of lumiracoxib (Table 1), which suggests that the substitution of chlorine at Position 6 of the 2-phenyl ring (lumiracoxib) with iodine (FIMA) does not greatly affect inhibitory potency or isoform selectivity. The K_i and IC_{50} values of lumiracoxib against COX-2 are reportedly better than or comparable to those of other COX-2 inhibitors including celecoxib [28]. FIMA showed better COX-2 inhibitory potency and isoform selectivity as compared with IMTP, an iodinated methyl sulfone-type analogue of celecoxib (IC_{50} for COX-2=5.16 μM; COX-1/COX-2 IC_{50} ratio>19) [22]. These results motivated us to further evaluate radioiodinated FIMA in in vitro cell uptake and in vivo biodistribution studies.

The in vitro cell uptake study showed that the accumulation level of ^{125}I-FIMA in COX-2 induced macrophages was significantly higher than in control macrophages and decreased with the addition of nonradioactive FIMA in a concentration dependent manner (Fig. 4). These results are indicative of a specific accumulation of ^{125}I-FIMA in COX-2 induced macrophages and are comparable to the recent results with ^{11}C-labeled 1,2-diarylpentens that demonstrated in vitro specificity for COX-2 [27]. In the biodistribution study in normal rats, ^{125}I-FIMA derived radioactivity cleared from all tissues and organs with the exception of the thyroid and intestine within the time period examined (Table 2). Notably, the radioactivity level in the blood was relatively low and showed rapid clearance. In addition, no significant ^{125}I-FIMA accumulation was observed in the stomach and thyroid which indicates that deiodination does not compromise the potentials of the labeled tracer. These results suggest the feasibility of the ^{123}I-labeled compound as a SPECT tracer for COX-2 expression.

Although COX-2 is an inducible isoform, it is found predominantly in the normal brain and kidneys [35]. Consistent with previous studies, a relatively high ^{125}I-FIMA accumulation was observed in the kidneys [14,22]. On the other hand, ^{125}I-FIMA showed little or no accumulation in the brain probably due to its lower lipophilicity ($logD_{7.4}$=1.84) as compared to other COX-2 inhibitors having a cyclic core with two vicinal aryl rings: ^{125}I-IMTP ($logD_{7.4}$=3.09), ^{125}I-IATP ($logD_{7.4}$=2.97 and ^{18}F-desbromo-DuP-697 ($logD_{7.4}$=3.72)[15]. ^{125}I-FIMA may not be a suitable candidate for COX-2 imaging in the brain.

Unfortunately, in the present study, we could not perform experiments to demonstrate in vivo specificity of the candidate compound. We generally perform experiments to block the uptake of a candidate compound in tissues by coinjection with the nonradioactive compound in order to confirm its specific distribution. Such blocking experiments, however, do not appear to be suitable for demonstrating the specific distribution of radiolabeled COX-2 inhibitors because the physiological expression levels of COX-2 are relatively low compared with those in the pathological state. In fact, McCarthy et al. [14] failed to obtain in vivo blocking data to show the specific binding of a radiotracer (^{18}F-SC58125) to COX-2 in rats. As de Vries et al. [24] have pointed out, it is debatable whether the lack of success of labeled COX-2 inhibitors is due to shortcomings of the tracers themselves or inadequate animal models that are used for their evaluation. Thus, it is still unclear whether the unique chemical structure and reduced lipophilicity of lumiracoxib are advantageous for the molecular imaging of COX-2. Experiments in animal models with higher and quantitative expression levels of COX-2 would be necessary to assess the specific binding of tracers to COX-2. Extensive studies to establish adequate animal models applicable to the assessment of COX-2 imaging tracers are greatly needed.

5. Conclusion

In the present study, we synthesized and evaluated the potential of radioiodinated FIMA, a derivative from the new generation COX-2 selective inhibitor, lumiracoxib, which is structurally distinct from other drugs in the class and has weakly acidic properties, as an imaging tracer. The radioiodination of FIMA was successfully achieved. The present results demonstrate FIMA has a high inhibitory potency and isoform selectivity for COX-2. Specific accumulation of ^{125}I-FIMA was observed in COX-2 induced macrophages, which indicates an in vitro specificity to COX-2. In addition, radioiodinated FIMA exhibited rapid blood clearance and no significant in vivo deiodination. These results indicate that radioiodinated FIMA meets the basic requirements for an effective radiotracer and can be a potential candidate as a SPECT tracer for COX-2 expression. Thus, radioiodinated FIMA deserves further investigation as a SPECT radiopharmaceutical for imaging COX-2 expression. Further experiments to demonstrate in vivo specificity of the labeled compound and comparative studies with previous COX-2 imaging tracers are needed.

Acknowledgments

This work was partly supported by a Grant-in-Aid for General Scientific Research from the Japan Society for the Promotion of Science.

References

[1] Davies NM, Good RL, Roupe KA, Yanez JA. Cyclooxygenase-3: axiom, dogma, anomaly, enigma or splice error? Not as easy as 1, 2, 3. J Pharm Sci 2004;7:217–26.
[2] Collaco-Moraes Y, Aspey B, Harrison M, de-Belleroche J. Cyclooxygenase-2 messenger RNA induction in focal cerebral ischemia. J Cereb Blood Flow Metab 1996;16:1366–72.
[3] FitzGerald GA. COX-2 and beyond: approaches to prostaglandin inhibition in human disease. Nat Rev Drug Discov 2003;2:879–90.
[4] Hara K, Kong DL, Sharp FR, Weinstein PR. Effect of selective inhibition of cyclooxygenase 2 on temporary focal cerebral ischemia in rats. Neurosci Lett 1998;256:53–6.

[5] Nogawa S, Zhang F, Ross ME, Iadecola C. Cyclo-oxygenase-2 gene expression in neurons contributes to ischemic brain damage. J Neurosci 1997;17:2746–55.
[6] Yokota C, Inoue H, Kuge Y, Abumiya T, Tagaya M, Hasegawa Y, et al. Cyclooxygenase-2 expression associated with spreading depression in a primate model. J Cereb Blood Flow Metab 2003;23:395–8.
[7] Yokota C, Kaji T, Kuge Y, Inoue H, Tamaki N, Minematsu K. Temporal and topographic profiles of cyclooxygenase-2 expression during 24 h of focal brain ishemia in rats. Neurosci Lett 2004;357: 219–22.
[8] Yokota C, Kuge Y, Inoue H, Tagaya M, Kito G, Susumu T, et al. Post-ischemic cyclooxygenase-2 expression is regulated by the extent of cerebral blood flow reduction in non-human primates. Neurosci Lett 2003;341:37–40.
[9] Yokota C, Kuge Y, Inoue H, Tamaki N, Minematsu K. Bilateral induction of the S-100A9 gene in response to spreading depression is modulated by the cyclooxygenase-2 activity. J Neurol Sci 2005;234: 11–6.
[10] Kaji T, Kuge Y, Yokota C, Tagaya M, Inoue H, Shiga T, et al. Characterisation of [^{123}I]iomazenil distribution in a rat model of focal cerebral ischaemia in relation to histopathological findings. Eur J Nucl Med Mol Imaging 2004;31:64–70.
[11] Kuge Y, Takai N, Ishino S, Temma T, Shiomi M, Saji H. Distribution profiles of membrane type-1 matrix metalloproteinase (MT1-MMP), matrix metalloproteinase-2 (MMP-2) and cyclooxygenase-2 (COX-2) in rabbit atherosclerosis: comparison with plaque instability analysis. Biol Pharm Bull 2007;30:1634–40.
[12] Herschman HR, Talley JJ, DuBois R. Cyclooxygenase 2 (COX-2) as a target for therapy and noninvasive imaging. Mol Imaging Biol 2003;5: 286–303.
[13] de Vries EF. Imaging of cyclooxygenase-2 (COX-2) expression: potential use in diagnosis and drug evaluation. Curr Pharm Des 2006; 12:3847–56.
[14] McCarthy TJ, Sheriff AU, Graneto MJ, Talley JJ, Welch MJ. Radiosynthesis, in vitro validation, and in vivo evaluation of 18F-labeled COX-1 and COX-2 inhibitors. J Nucl Med 2002;43:117–24.
[15] de Vries EF, van Waarde A, Buursma AR, Vaalburg W. Synthesis and in vivo evaluation of 18F-desbromo-DuP-697 as a PET tracer for cyclooxygenase-2 expression. J Nucl Med 2003;44:1700–6.
[16] Wust FR, Hohne A, Metz P. Synthesis of ^{18}F-labelled cyclooxygenase-2 (COX-2) inhibitors via Stille reaction with 4-[^{18}F]fluoroiodobenzene as radiotracers for positron emission tomography (PET). Org Biomol Chem 2005;3:503–7.
[17] Majo VJ, Prabhakaran J, Simpson NR, Van Heertum RL, Mann JJ, Kumar JS. A general method for the synthesis of aryl [^{11}C] methylsulfones: potential PET probes for imaging cyclooxygenase-2 expression. Bioorg Med Chem Lett 2005;15:4268–71.
[18] Prabhakaran J, Majo VJ, Simpson NR, Van Heertum RL, Mann JJ, Kumar JS. Synthesis of [C-11]celecoxib: a potential PET probe for imaging COX-2 expression. J Label Compd Radiopharm 2005;48: 887–95.
[19] Toyokuni T, Kumar JS, Walsh JC, Shapiro A, Talley JJ, Phelps ME, et al. Synthesis of 4-(5-[^{18}F]fluoromethyl-3-phenylisoxazol-4-yl)benzenesulfonamide, a new [^{18}F]fluorinated analogue of valdecoxib, as a potential radiotracer for imaging cyclooxygenase-2 with positron emission tomography. Bioorg Med Chem Lett 2005;15:4699–702.
[20] Yang DJ, Bryant J, Chang JY, Mendez R, Oh CS, Yu DF, et al. Assessment of cyclooxygense-2 expression with ^{99}mTc-labeled celebrex. Anticancer Drugs 2004;15:255–63.
[21] Kabalka GW, Mereddy AR, Schuller HM. Synthesis of an iodine-123-labeled celecoxib analogue: a potential spect agent. J Label Compd Radiopharm 2005;48:295–300.
[22] Kuge Y, Katada Y, Shimonaka S, Temma T, Kimura H, Kiyono Y, et al. Synthesis and evaluation of radioiodinated cyclooxygenase-2 inhibitors as potential SPECT tracers for cyclooxygenase-2 expression. Nucl Med Biol 2006;33:21–7.
[23] Prabhakaran J, Underwood MD, Parsey RV, Arango V, Majo VJ, Simpson NR, et al. Synthesis and in vivo evaluation of [^{18}F]-4-[5-(4-methylphenyl)-3-(trifluoromethyl)-1*H*-pyrazol-1-yl]benzenesul fonamide as a PET imaging probe for COX-2 expression. Bioorg Med Chem 2007;15:1802–7.
[24] de Vries EF, Doorduin J, Dierckx RA, van Waarde A. Evaluation of [(11)C]rofecoxib as PET tracer for cyclooxygenase 2 overexpression in rat models of inflammation. Nucl Med Biol 2008;35:35–42.
[25] Tian H, Lee Z. Synthesis of ^{18}F-labeled cyclooxygenase-2 (COX-2) inhibitor as a potential PET imaging agent. J Label Compd Radiopharm 2006;49:583–93.
[26] Tanaka M, Fujisaki Y, Kawamura K, Ishiwata K, Qinggeletu, Yamamoto F, et al. Radiosynthesis and evaluation of 11C-labeled diaryl-substituted imidazole and indole derivatives for mapping cyclooxygenase-2. Biol Pharm Bull 2006;29:2087–94.
[27] Wuest F, Kniess T, Bergmann R, Pietzsch J. Synthesis and evaluation in vitro and in vivo of a 11C-labeled cyclooxygenase-2 (COX-2) inhibitor. Bioorg Med Chem 2008;16:7662–70.
[28] Esser R, Berry C, Du Z, Dawson J, Fox A, Fujimoto RA, et al. Preclinical pharmacology of lumiracoxib: a novel selective inhibitor of cyclooxygenase-2. Br J Pharmacol 2005;144:538–50.
[29] Stichtenoth DO, Frolich JC. The second generation of COX-2 inhibitors: what advantages do the newest offer? Drugs 2003;63: 33–45.
[30] Buvanendran A, Barkin R. Lumiracoxib. Drugs Today (Barc) 2007;43: 137–47.
[31] Bannwarth B, Berenbaum F. Clinical pharmacology of lumiracoxib, a second-generation cyclooxygenase 2 selective inhibitor. Expert Opin Investig Drugs 2005;14:521–33.
[32] Rordorf CM, Choi L, Marshall P, Mangold JB. Clinical pharmacology of lumiracoxib: a selective cyclo-oxygenase-2 inhibitor. Clin Pharmacokinet 2005;44:1247–66.
[33] Acemoglu M, Allmendinger T, Calienni J, Cercus J, Loiseleur O, Sedelmeier GH, et al. Synthesis of new *N*-aryl oxindoles as intermediates for pharmacologically active compounds. Tetrahedron 2004;60:11571–86.
[34] Katsuyama M, Ikegami R, Karahashi H, Amano F, Sugimoto Y, Ichikawa A. Characterization of the LPS-stimulated expression of EP2 and EP4 prostaglandin E receptors in mouse macrophage-like cell line, J774.1. Biochem Biophys Res Commun 1998;251:727–31.
[35] Kam PC, See AU. Cyclo-oxygenase isoenzymes: physiological and pharmacological role. Anaesthesia 2000;55:442–9.

6394 J. Med. Chem. 2009, 52, 6394–6401
DOI: 10.1021/jm901057p

Journal of
Medicinal
Chemistry
Article

Fluoro-pegylated Chalcones as Positron Emission Tomography Probes for in Vivo Imaging of β-Amyloid Plaques in Alzheimer's Disease

Masahiro Ono,*,†,‡ Rumi Watanabe,† Hidekazu Kawashima,§ Yan Cheng,‡ Hiroyuki Kimura,‡ Hiroyuki Watanabe,† Mamoru Haratake,† Hideo Saji,‡ and Morio Nakayama*,†

†*Department of Hygienic Chemistry, Graduate School of Biomedical Sciences, Nagasaki University, 1-14 Bunkyo-machi, Nagasaki 852-8521, Japan,* ‡*Department of Patho-Functional Bioanalysis, Graduate School of Pharmaceutical Sciences, Kyoto University, Yoshida Shimoadachi-cho, Sakyo-ku, Kyoto 606-8501, Japan, and* §*Department of Nuclear Medicine and Diagnostic Imaging, Graduate School of Medicine, Kyoto University, Shogoin Kawahara-cho, Sakyo-ku, Kyoto 606-8507, Japan*

Received July 16, 2009

This paper describes the synthesis and biological evaluation of fluoro-pegylated (FPEG) chalcones for the imaging of β-amyloid (Aβ) plaques in patients with Alzheimer's disease (AD). FPEG chalcone derivatives were prepared by the aldol condensation reaction. In binding experiments conducted in vitro using Aβ(1−42) aggregates, the FPEG chalcone derivatives having a dimethylamino group showed higher K_i values (20−50 nM) than those having a monomethylamino or a primary amine group. When the biodistribution of ^{11}C-labeled FPEG chalcone derivatives having a dimethyamino group was examined in normal mice, all four derivatives were found to display sufficient uptake for imaging Aβ plaques in the brain. ^{18}F-labeled **7c** also showed good uptake by and clearance from the brain, although a slight difference between the ^{11}C and ^{18}F tracers was observed. When the labeling of Aβ plaques was carried out using brain sections of AD model mice and an AD patient, the FPEG chalcone derivative **7c** intensely labeled Aβ plaques. Taken together, the results suggest **7c** to be a useful candidate PET tracer for detecting Aβ plaques in the brain of patients with AD.

Introduction

The formation of β-amyloid (Aβ[a]) plaques is a key neurodegenerative event in Alzheimer's disease (AD).[1,2] Because the imaging of Aβ plaques in vivo may lead to the presymptomatic diagnosis of AD, many radiotracers that bind to Aβ plaques have been developed.[3,4] Preliminary reports of positron emission tomography (PET) suggested that the uptake and retention of 2-(4′-[^{11}C]methylaminophenyl)-6-hydroxybenzothiazole ([^{11}C]PIB, **1**)[5,6] and 4-*N*-[^{11}C]methylamino-4′-hydroxystilbene ([^{11}C]SB-13, **2**)[7,8] differed between the brain of AD patients and those of controls. However, because ^{11}C is a positron-emitting isotope with a $t_{1/2}$ of just 20 min, efforts are being made to develop comparable agents labeled with the isotope ^{18}F ($t_{1/2}$ = 110 min). [^{18}F]-2-(1-(2-(*N*-(2-fluoroethyl)-*N*-methylamino)-naphthalene-6-yl)ethylidene)malononitrile ([^{18}F]FDDNP, **3**)[9,10] and [^{18}F]-4-(*N*-methylamino)-4′-(2-(2-(2-fluoroethoxy)ethoxy)ethoxy)-stilbene ([^{18}F]BAY94−9172, **4**)[11,12] should be useful as tracers for imaging Aβ plaques in the diagnosis of AD. Recent reports suggest that Aβ aggregates possess multiple ligand-binding sites, the density of which differs.[13−15] Therefore, the development of novel probes that bind Aβ aggregates may lead to critical findings regarding the pathology of AD.

Recently, in a search for novel Aβ-imaging probes, we found that radioiodinated flavone,[16,17] chalcone,[18,19] and aurone[20,21] derivatives, which are categorized as flavonoids, showed excellent characteristics such as high affinity for Aβ aggregates and good uptake into and rapid clearance from the brain. The chalcone structure in particular is considered to be a useful core in the development of new Aβ-imaging probes because it can be formed by a one-pot condensation reaction. In addition, because chalcone derivatives show different characteristics of binding to Aβ aggregates from Congo Red and thioflavin T, they are expected to provide new information from in vivo imaging in AD brains.

In the present study, we designed and synthesized fluorinated chalcone derivatives for the purpose of developing ^{18}F-labeled probes for PET-based imaging of Aβ plaques. The formation of bioconjugates based on pegylation-fluorination resulting in fluoro-pegylated (FPEG) molecules is effective for some core structures of Aβ-imaging probes.[22] We have adopted a novel approach, adding a short PEG (n = 1−3) to the chalcone backbone and capping the end of the ethylene glycol chain with a fluorine atom. Indeed, the most promising ^{18}F-labeled agent **4** possesses PEG (n = 3) in the stilbene backbone. This tracer showed strong affinity (K_i = 6.7 nM) for Aβ plaques, high uptake (7.77%ID/g at 2 min postinjection), and rapid clearance from the mouse brain

*To whom correspondence should be addressed. For M.O.: phone, +81-75-753-4608; fax, +81-75-753-4568; E-mail, ono@pharm.kyoto-u.ac.jp. For M.N.: phone, +81-95-819-2441; fax, +81-95-819-2441; E-mail: morio@nagasaki-u.ac.jp.

[a] Abbreviations: Aβ, β-amyloid; AD, Alzheimer's disease; PET, positron emission tomography; PIB, 2-(4′-methyaminophenyl)-6-hydroxybenzothiazole; SB-13, 4-*N*-methylamino-4′-hydroxystilbene; FDDNP, 2-(1-(2-(*N*-(2-fluoroethyl)-*N*-methylamino)naphthalene-6-yl)ethylidene)-malononitrile; BAY94-9174, 4-(*N*-methylamino)-4′-(2-(2-(2-fluoroethoxy)ethoxy)ethoxy)-stilbene; DMIC, 4-dimethylamino-4′-iodo-chalcone; IMPY, 6-iodo-2-(4′-dimethylamino)phenyl-imidazo[1,2-*a*]pyridine; FPEG, fluoro-pegylated; DAST, diethylamino sulfur trifluoride; DME, 1,2-dimethoxyethane; MEK, methyl ethyl ketone; [^{11}C]methyl triflate, [^{11}C]MeOTf; DAB, 3,3′-diaminobenzidine.

pubs.acs.org/jmc Published on Web 09/16/2009

Scheme 1

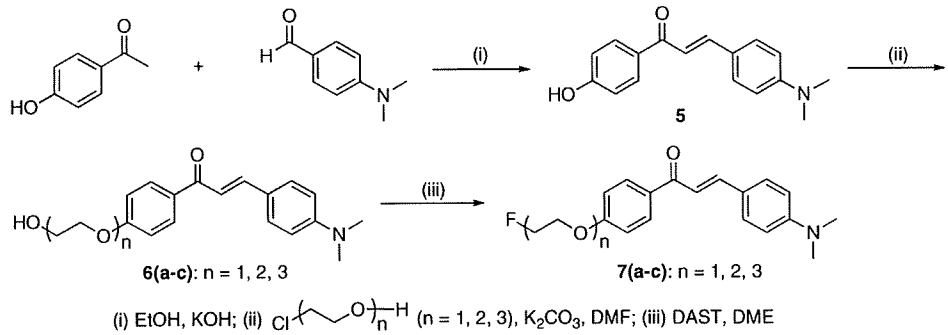

Scheme 2

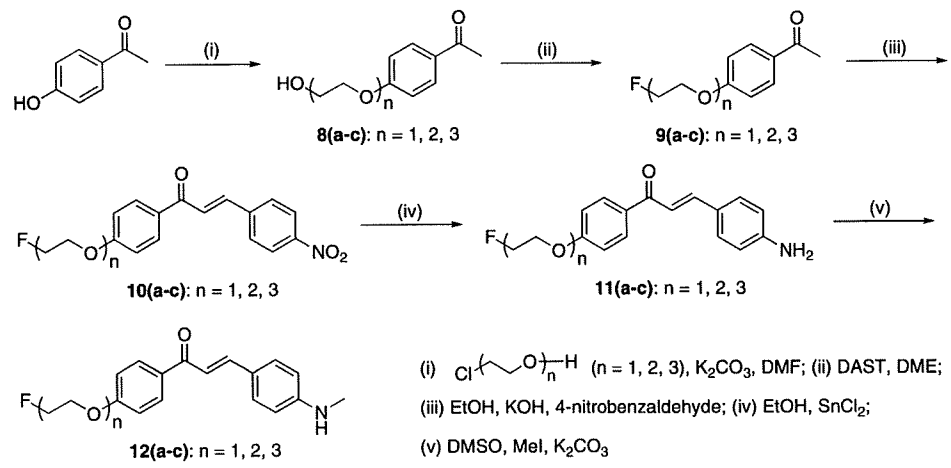

Scheme 3[a]

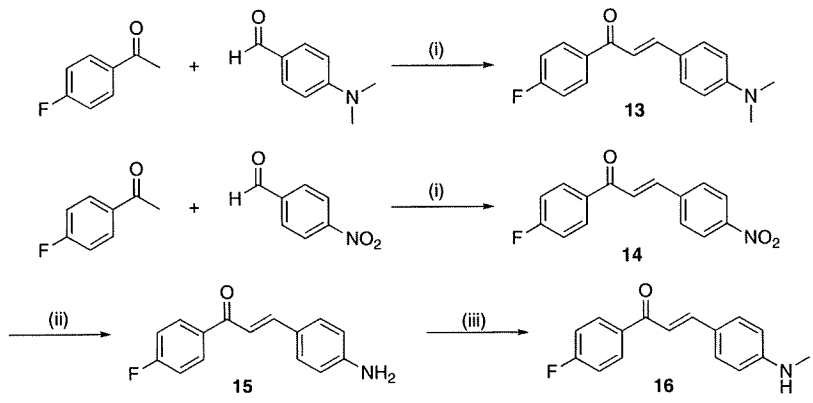

[a] (i) EtOH, KOH; (ii) EtOH, $SnCl_2$; (iii) DMSO, MeI, K_2CO_3.

(1.61%ID/g at 60 min postinjection).[12] We adopted the biological data for **4** as criteria to develop novel Aβ-imaging agents. In this study, we synthesized 12 fluorinated chalcones and evaluated their biological potential as Aβ-imaging agents by testing their affinity for Aβ aggregates and Aβ plaques in sections of brain tissue from AD model mice and an AD patient and their uptake by and clearance from the brain in biodistribution experiments using normal mice.

Results and Discussion

The synthesis of the FPEG chalcone derivatives is outlined in Schemes 1, 2, and 3. The most useful way to prepare chalcones is the condensation of acetophenones with ben zaldehydes. Using this process, 4-hydroxyacetophenone or 4-fluoroacetophenone was reacted with 4-dimethylaldehyde to form 4′-hydroxy-4-dimethylamino-chalcone **5** and 4′-fluoro-4-dimethylamino-chalcone **13** in yields of 84.0 and 41.6%, respectively. Compounds **10(a−c)** were synthesized by an aldol reaction between FPEG acetophenone **9(a−c)** and 4-nitrobenzaldehyde. Fluorination of **6(a−c)** and **8(a−c)** to prepare **7(a−c)** and **9(a−c)** was done using diethylamino sulfur trifluoride (DAST) after introducing three oligoethylene glycol molecules into the phenolic OH of **5** and **9(a−c)**. The amino derivatives **11(a−c)** and **15** were readily prepared from **10(a−c)** and **14** by reduction with $SnCl_2$. Conversion of **11(a−c)** and **15** to the monomethylamino derivatives **12(a−c)** and **16** was achieved by methylation with CH_3I under alkaline conditions. Preparation of ^{11}C-labeled compounds was done as in Scheme 4. ^{11}C-labeled chalcones

Scheme 4

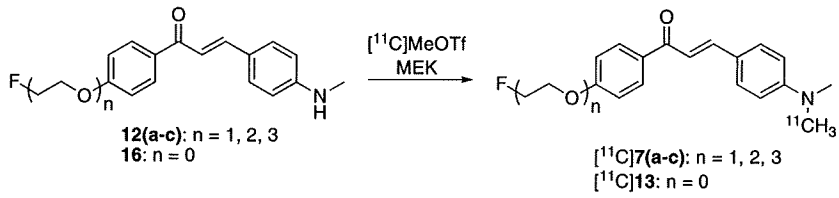

Scheme 5

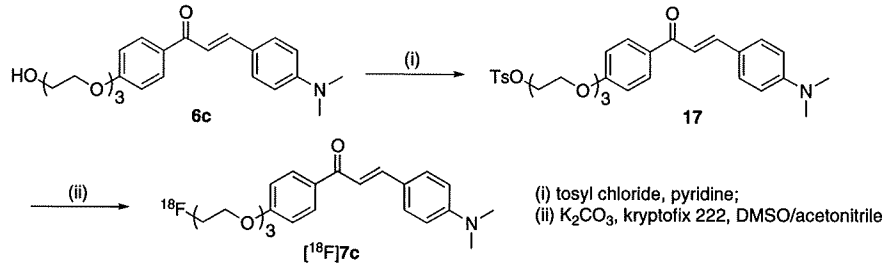

Table 1. Chemical Structures and Inhibition Constants of Fluorinated Chalcone Derivatives

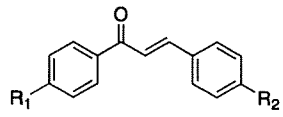

compd	R_1	R_2	K_i (nM)[a]
7a	FCH_2CH_2O	$N(CH_3)_2$	45.7 ± 7.1
7b	$F(CH_2CH_2O)_2$	$N(CH_3)_2$	20.0 ± 2.5
7c	$F(CH_2CH_2O)_3$	$N(CH_3)_2$	38.9 ± 4.2
11a	FCH_2CH_2O	NH_2	678.9 ± 21.7
11b	$F(CH_2CH_2O)_2$	NH_2	1048.0 ± 114.3
11c	$F(CH_2CH_2O)_3$	NH_2	790.0 ± 132.1
12a	FCH_2CH_2O	$NHCH_3$	197.1 ± 58.8
12b	$F(CH_2CH_2O)_2$	$NHCH_3$	216.4 ± 13.8
12c	$F(CH_2CH_2O)_3$	$NHCH_3$	470.9 ± 100.4
13	F	$N(CH_3)_2$	49.8 ± 6.2
15	F	NH_2	663.0 ± 88.3
16	F	$NHCH_3$	234.2 ± 44.0
DMIC	I	$N(CH_3)_2$	13.1 ± 3.0
IMPY			28.0 ± 4.1

[a] Inhibition constants (K_i, nM) of compounds for the binding of [^{125}I]DMIC to Aβ(1−42) aggregates. Values are the mean ± standard error of the mean for 4−9 independent experiments.

were readily synthesized from their *N*-normethyl precursors, **12(a−c)** and **16**, and [^{11}C]methyl triflate ([^{11}C]-MeOTf). Radiochemical yields of the final product were 28−35%, decay corrected to end of bombardment. Radiochemical purity was >99% with a specific activity of 22−28 GBq/μmol. The identity of [^{11}C]**7a**, [^{11}C]**7b**, [^{11}C]**7c**, and [^{11}C]**13** was confirmed by a comparison of HPLC retention times with the nonradioactive compounds (**7a**, **7b**, **7c**, and **13**). ^{18}F labeling of **7c** was performed on a tosyl precursor **17** undergoing a nucleophilic displacement reaction with the fluoride anion (Scheme 5). Radiolabeling with ^{18}F was successfully performed on the precursor to generate [^{18}F]**7c** with a radiochemical yield of 45% and radiochemical purity >99%. The identity of [^{18}F]**7c** was verified by a comparison of retention time with the nonradioactive compound. The specific activity of [^{18}F]**7c** was estimated to be 35 GBq/mmol at the end of synthesis.

Table 2. Biodistribution of Radioactivity after Injection of [^{11}C]**7a**, [^{11}C]**7b**, [^{11}C]**7c**, and [^{11}C]**13** in Normal Mice[a]

organ	2 min	10 min	30 min	60 min
		[^{11}C]**7a**		
blood	3.65 ± 0.37	2.73 ± 0.28	2.12 ± 0.18	2.22 ± 0.25
brain	6.01 ± 0.61	3.24 ± 0.39	2.57 ± 0.26	2.26 ± 0.41
		[^{11}C]**7b**		
blood	3.48 ± 0.56	2.28 ± 0.84	2.54 ± 0.96	1.44 ± 0.36
brain	4.73 ± 0.47	2.23 ± 0.18	1.14 ± 0.12	1.00 ± 0.19
		[^{11}C]**7c**		
blood	2.44 ± 0.25	1.52 ± 0.42	1.01 ± 0.15	0.68 ± 0.10
brain	4.31 ± 0.33	1.38 ± 0.16	0.64 ± 0.07	0.35 ± 0.03
		[^{11}C]**13**		
blood	2.61 ± 0.35	1.60 ± 0.25	0.39 ± 0.05	1.40 ± 0.20
brain	3.68 ± 0.35	1.53 ± 0.14	1.04 ± 0.15	1.04 ± 0.20

[a] Expressed as % of injected dose per gram. Each value represents the mean ± SD for 4−5 mice.

Table 3. Biodistribution of Radioactivity after Injection of [^{18}F]**7c** in Normal Mice[a]

organ	2 min	10 min	30 min	60 min
blood	2.09 ± 0.40	1.94 ± 0.18	2.35 ± 0.33	1.87 ± 0.26
brain	3.48 ± 0.47	1.52 ± 0.03	1.08 ± 0.09	1.07 ± 0.17
bone	1.80 ± 0.31	1.76 ± 0.15	2.98 ± 0.49	3.58 ± 0.41

[a] Expressed as % of injected dose per gram. Each value represents the mean ± SD for 4−5 mice.

Experiments in vitro to evaluate the affinity of the FPEG chalcones for Aβ aggregates were carried out in solutions of Aβ aggregates with [^{125}I]4-dimethylamino-4′-iodo-chalcone ([^{125}I]DMIC)[18] as the ligand (Table 1). The K_i values suggested that the binding to Aβ(1−42) aggregates was affected by substitution at the amino group at position 4 in the chalcone structure, not by the length of PEG introduced into the chalcone backbone. The fluorinated chalcones had binding affinity for Aβ(1−42) aggregates in the following order: the dimethyamino derivatives (**7a**, **7b**, **7c**, and **13**) > the monomethylamino derivatives (**12a**, **12b**, **12c**, and **16**) > the primary amino derivatives (**11a**, **11b**, **11c**, and **15**). The result of the binding experiments is consistent with that of previous reports.[16,19] In addition, the affinity of the dimethylamino

Figure 1. Neuropathological staining of 10 μm sections of a Tg2576 mouse brain (A and B) and aged normal brain (C). Fluorescent staining of compound **7c** in the Tg2576 mouse brain (A). Aβ immunostaining with antibody BC05 in the adjacent section (B). Fluorescent staining of compound **7c** in the age-matched control mouse brain (C).

derivatives was in the same range as that of the known compound, 6-iodo-2-(4′-dimethylamino)phenyl-imidazo[1,2-*a*]pyridine (IMPY), which is commonly used for inhibition assays.[22−25] We selected the dimethylamino derivatives (**7a**, **7b**, **7c**, and **13**), which showed the greatest affinity, for additional studies.

To evaluate brain uptake of the FPEG chalcones, biodistribution experiments were performed in normal mice with four ^{11}C-labeled FPEG chalcones ([^{11}C]**7a**, [^{11}C]**7b**, [^{11}C]**7c**, and [^{11}C]**13**) (Table 2). Because normal mice were used for the biodistribution experiments, no Aβ plaques were expected in the young mice; therefore the washout of probes from the brain should be rapid to obtain a higher signal-to-noise ratio earlier in the AD brain. Radioactivity after injection of the ^{11}C-labeled FPEG chalcones penetrated the blood−brain barrier, showing excellent uptake ranging from 3.7 to 6.0% ID/g brain at 2 min postinjection, a level sufficient for imaging Aβ plaques in the brain. In addition, they displayed good clearance from the normal brain with 2.3, 1.0, 0.35, and 1.0% ID/g at 60 min postinjection for [^{11}C]**7a**, [^{11}C]**7b**, [^{11}C]**7c**, and [^{11}C]**13**, respectively. These values were equal to 37.6, 21.1, 8.1, and 28.3% of the initial uptake peak for [^{11}C]**7a**, [^{11}C]**7b**, [^{11}C]**7c**, and [^{11}C]**13**, respectively. Compound **7c** with the fastest washout from the brain was labeled with ^{18}F and evaluated for its biodistribution in normal mice (Table 3). [^{18}F]**7c** displayed high uptake (3.48%ID/g) at 2 min postinjection, a level sufficient for imaging like [^{11}C]**7c**, and was cleared over the subsequent 10, 30, and 60 min. The radioactivity in the brain at 60 min postinjection was 1.07%ID/g, indicating that this [^{18}F]**7c** has favorable pharmacokinetics in the brain. Although we consider that a slight difference of the radioactivity pharmacokinetics between [^{11}C]**7c** and [^{18}F]**7c** could be attributable to the different physicochemical characteristics of their radiometabolites produced in the brain, the reason for this difference has remained unclear. Bone uptake at 60 min was measurable (3.58%ID/g), suggesting defluorination in vivo. Bone uptake has been observed for other ^{18}F tracers.[12,22−24] However, previous reports suggested that free fluoride was not taken up by brain tissue; therefore, the interference from free fluoride may be relatively low for brain imaging. A previous paper regarding the most promising ^{18}F-labeled agent **4** reported that it showed high uptake (7.77% ID/g at 2 min postinjection) and rapid clearance from the brain (1.61%ID/g at 60 min postinjection) with little accumulation in bone (1.77%ID/g at 60 min postinjection) in biodistribution experiments using normal mice.[12] The pharmacokinetics of **4** appear superior to that of [^{18}F]**7c**, but the good biological results obtained with [^{18}F]**7c** suggest that further investigation is warranted.

To investigate the ability of the fluorinated chalcones to bind to Aβ plaques in the AD model, fluorescent staining of sections of mouse brain were carried out with compound **7c** (Figure 1). We used Tg2576 transgenic mice as an animal model of Aβ plaque deposition, which express human APP695 with the K670N, M671L Swedish double mutation.[26] By 11−13 months of age, Tg2576 mice show prominent Aβ deposition in the cingulated cortex, entorhinal cortex, dentate gyrus, and CA1 hippocampal subfield and have been frequently used for the evaluation of specific binding of Aβ plaques in in vitro and in vivo experiments.[12,24,27−31] Many Aβ plaques were clearly stained with **7c**, as reflected by the affinity for the aggregates of synthetic Aβ(1−42) in in vitro competition assays (Figure 1A). The labeling pattern was consistent with that observed after immunohistochemical labeling by BC05, a specific antibody for Aβ (Figure 1B), while wild-type mouse brain displayed no significant accumulation of **7c** (Figure 1C). The results indicated that **7c** binds specifically to Aβ plaques in Tg2576 mice brain. A previous report suggested the configuration/folding of Aβ plaques in Tg2576 mice to be different from the tertiary/quaternary structure of Aβ plaques in AD brains.[30,32] In addition, the studies reported with **1** further indicate that the binding of **1** reflects the amount of Aβ plaques in human AD brain but not in Tg2576 mouse brain, and the detectability of Aβ plaques by **1** is dependent on the accumulation of specific Aβ subtypes.[28,29] Therefore, we considered that it should be essential to evaluate the binding affinity for Aβ plaques in human AD brains because our goal is to develop clinically useful probes for in vivo imaging of Aβ plaques in humans.

Next, we investigated the binding affinity of [^{18}F]**7c** for Aβ plaques by in vitro autoradiography in a human AD brain section (Figure 2A). The autoradiographic image of [^{18}F]**7c** showed high levels of radioactivity in some specific areas of the brain section. Furthermore, we confirmed that the hot spots of [^{18}F]**7c** in an AD brain section corresponded with those of in vitro thioflavin-S staining in the same brain section (Figure 2B). In contrast, no significant accumulation of [^{18}F]**7c** was observed in the region without Aβ plaques (Figure 2C). The results demonstrate the feasibility of using [^{18}F]**7c** as a probe for detecting Aβ plaques in the brain of AD patients with PET.

In conclusion, we reported novel FPEG chalcone derivatives, containing an end-capped fluoropolyethylene glycol as in vivo PET imaging agents for Aβ plaques in the brain. The FPEG chalcones with a dimethylamino group displayed greater affinity for synthetic Aβ aggregates than did the monomethylamino and primary amino derivatives. In biodistribution experiments using normal mice, ^{11}C-labeled FPEG chalcones displayed sufficient uptake for the imaging of Aβ plaques in the brain. [^{11}C]**7c** showed the fastest clearance from the brain, probably related to a low nonspecific binding. [^{18}F]**7c** also displayed high uptake in and good clearance from

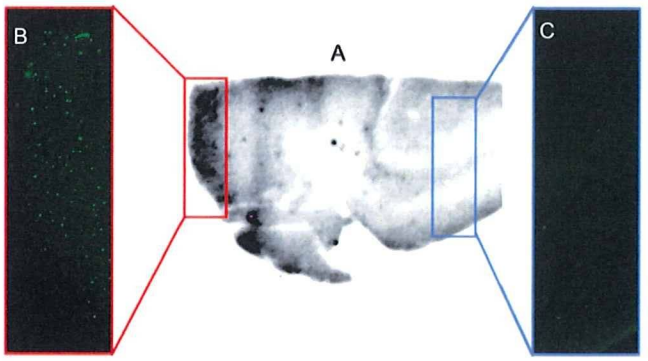

Figure 2. In vitro autoradiography of [^{18}F]**7c** using the human AD brain section (A). Aβ plaques were confirmed by in vitro staining of the same section with thioflavin-S (B and C).

the brain, although a slight difference was observed between the ^{11}C and ^{18}F tracers. When the labeling of plaques in vitro was carried out using sections of brain tissue from an animal model of AD and an AD patient, compound **7c** intensely labeled Aβ plaques existing in both brains. Taken together, the results suggest the novel FPEG chalcone **7c** to be potentially useful for imaging Aβ plaques in the brain using PET.

Experimental Section

General. All reagents were obtained commercially and used without further purification unless otherwise indicated. ^{1}H NMR spectra were obtained on a Varian Gemini 300 spectrometer with TMS as an internal standard. Coupling constants are reported in hertz. Multiplicity was defined by s (singlet), d (doublet), t (triplet) and m (multiplet). Mass spectra were obtained on a JEOL IMS-DX instrument. HPLC analysis was performed on a Shimadzu HPLC system (a LC-10AT pump with a SPD-10A UV detector, $\lambda = 254$ nm) using a Cosmosil C_{18} column (Nakalai Tesque, 5C_{18}-AR-II, 4.6 mm × 150 mm) using acetonitrile/water (50/50) as mobile phase at a flow rate of 1.0 mL/min. All key compounds were proven by this method to show ≥95% purity.

Chemistry. (*E*)-3-(4-(Dimethylamino)phenyl)-1-(4-hydroxyphenyl)-2-propen-1-one (5). 4-Hydroxyacetophenone (1.36 g, 10 mmol) and 4-dimethylaminobenzaldehyde (1.86 g, 10.0 mmol were dissolved in EtOH (15 mL). A 30 mL aliquot of a 10% aqueous KOH solution was then slowly added dropwise to the reaction mixture. The mixture was stirred for 24 h at 100 °C and then extracted with ethyl acetate. After the organic layers were combined and dried over Na_2SO_4, evaporation of the solvent afforded 1.50 g of **5** (84.0%). ^{1}H NMR (CD_3OD) δ: 3.04 (s, 6H), 6.76 (d, $J = 8.7$ Hz, 2H), 6.88 (d, $J = 8.7$ Hz, 2H), 7.50 (d, $J = 15.3$ Hz, 1H), 7.59 (d, $J = 9.0$ Hz, 2H), 7.72 (d, $J = 15.3$ Hz, 1H), 7.98 (d, $J = 8.7$ Hz, 2H). ^{1}H NMR (DMSO-d_6) δ: 2.99 (s, 6H), 6.74 (d, $J = 8.7$ Hz, 2H), 6.88 (d, $J = 8.4$ Hz, 2H), 7.62 (s, 2H), 7.68 (d, $J = 8.7$ Hz, 2H), 8.03 (d, $J = 8.7$ Hz, 2H), 10.30 (s, 1H). EI-MS: m/z 267 (M^+).

(*E*)-3-(4-(Dimethylamino)phenyl)-1-(4-(2-hydroxyethoxy)phenyl)-2-propen-1-one (6a). To a solution of **5** (500 mg, 1.87 mmol and ethylene chlorohydrin (125 μL, 1.87 mmol) in DMSO (5 mL) was added anhydrous K_2CO_3 (775 mg, 5.61 mmol). The reaction mixture was stirred for 18 h at 100 °C and then poured into water and extracted with chloroform. The organic layers were combined and dried over Na_2SO_4. Evaporation of the solvent afforded a residue, which was purified by silica gel chromatography (hexane: ethyl acetate = 1:1) to give 422 mg of **6a** (72.7%). ^{1}H NMR ($CDCl_3$) δ: 3.04 (s, 6H), 4.00−4.01 (m, 2H), 4.17 (t, $J = 4.8$ Hz, 2H), 6.69 (d, $J = 9.0$ Hz, 2H), 6.99 (d, $J = 6.9$ Hz, 2H), 7.35 (d, $J = 15.3$ Hz, 1H), 7.55 (d, $J = 9.0$ Hz, 2H), 7.79 (d, $J = 15.3$ Hz, 1H), 8.02 (d, $J = 9.3$ Hz, 2H).

(*E*)-3-(4-(Dimethylamino)phenyl)-1-(4-(2-(hydroxyethoxy)ethoxy)-phenyl)-2-propen-1-one (6b). The reaction described above to prepare **6a** was used, and **6b** was obtained from **5** and ethylene glycol mono-2-chloroethyl ether. ^{1}H NMR ($CDCl_3$) δ: 3.05 (s, 6H), 3.69 (t, $J = 4.8$ Hz, 2H), 3.78 (s, 2H), 3.91 (t, $J = 4.8$ Hz, 2H), 4.23 (t, $J = 4.8$ Hz, 2H), 6.70 (d, $J = 9.0$ Hz, 2H), 6.99 (d, $J = 9.0$ Hz, 2H), 7.35 (d, $J = 15.3$ Hz, 1H), 7.55 (d, $J = 8.7$ Hz, 2H), 7.79 (d, $J = 15.6$ Hz, 1H), 8.02 (d, $J = 9.0$ Hz, 2H).

(*E*)-3-(4-(Dimethylamino)phenyl)-1-(4-(2-((hydroxyethoxy)ethoxy)-ethoxy)phenyl)-2-propen-1-one (6c). The reaction described above to prepare **6a** was used, and 429 mg of **6c** was obtained in a yield of 82.6% from **5** and 2-[2-(2-chloroethoxy)-ethoxy]ethanol. ^{1}H NMR ($CDCl_3$) δ: 3.04 (s, 6H), 3.62 (t, $J = 5.1$ Hz, 2H), 3.73−3.75 (m, 6H), 3.90 (t, $J = 4.8$ Hz, 2H), 4.22 (t, $J = 4.8$ Hz, 2H), 6.70 (d, $J = 9.0$ Hz, 2H), 6.99 (d, $J = 8.7$ Hz, 2H), 7.35 (d, $J = 15.3$ Hz, 1H), 7.55 (d, $J = 9.0$ Hz, 2H), 7.78 (d, $J = 15.3$ Hz, 1H), 8.02 (d, $J = 9.0$ Hz, 2H).

(*E*)-3-(4-(Dimethylamino)phenyl)-1-(4-(2-fluoroethoxy)phenyl)-2-propen-1-one (7a). To a solution of **6a** (100 mg, 0.32 mmol in 1,2-dimethoxyethane (DME) (5 mL) was added DAST (85 μL, 0.64 mmol) in a dry ice−acetone bath. The reaction mixture was stirred for 1 h at room temperature and then poured into a saturated $NaHSO_3$ solution and extracted with chloroform. After the organic phase was separated, dried over Na_2SO_4, and filtered, and the residue was purified by preparative TLC (hexane:ethyl acetate = 3:1) to give 39 mg of **7a** (38.9%). ^{1}H NMR ($CDCl_3$) δ: 3.09 (s, 6H), 4.30 (d, t, $J_1 = 27.6$ Hz, $J_2 = 4.2$ Hz, 2H), 4.79 (d, t, $J_1 = 47.4$ Hz, $J_2 = 4.2$ Hz, 2H), 6.70 (d, $J = 8.7$ Hz, 2H), 7.00 (d, $J = 9.0$ Hz, 2H), 7.35 (d, $J = 15.6$ Hz, 1H), 7.55 (d, $J = 9.0$ Hz, 2H), 7.79 (d, $J = 15.3$ Hz, 1H), 8.03 (d, $J = 9.0$ Hz, 2H). EI-MS: m/z 313 (M^+).

(*E*)-3-(4-(Dimethylamino)phenyl)-1-(4-(2-(fluoroethoxy)ethoxy)-phenyl)-2-propen-1-one (7b). The reaction described above to prepare **7a** was used, and 28 mg of **7b** was obtained in a yield of 28.0% from **6b**. ^{1}H NMR ($CDCl_3$) δ: 3.04 (s, 6H), 3.77−3.94 (m, 4H), 4.21−4.24 (m, 3H), 4.61 (d, t, $J_1 = 47.4$ Hz, $J_2 = 4.2$ Hz 1H), 6.69 (d, $J = 9.3$ Hz, 2H), 6.99 (d, $J = 8.7$ Hz, 2H), 7.35 (d, $J = 15.3$ Hz, 2H), 7.55 (d, $J = 9.0$ Hz, 2H), 7.78 (d, $J = 15.6$ Hz, 2H), 8.02 (d, $J = 9.0$ Hz, 2H). EI-MS: m/z 357 (M^+).

(*E*)-3-(4-(Dimethylamino)phenyl)-1-(4-(2-((fluoroethoxy)ethoxy)-ethoxy)phenyl)-2-propen-1-one (7c). The reaction described above to prepare **7a** was used, and 29 mg of **7c** was obtained in a yield of 14.4% from **6c** and 2-[2-(2-chloroethoxy)ethoxy]ethanol. ^{1}H NMR ($CDCl_3$) δ: 3.04 (s, 6H), 3.73−3.81 (m, 6H), 3.90 (t, $J = 5.1$ Hz, 2H), 4.21 (t, $J = 5.1$ Hz, 2H), 4.49 (t, $J = 4.5$ Hz, 1H), 4.65 (t, $J = 4.5$ Hz, 1H), 6.70 (d, $J = 8.7$ Hz, 2H), 6.98 (d, $J = 9.0$ Hz, 2H), 7.35 (d, $J = 15.3$ Hz, 1H), 7.55 (d, $J = 8.7$ Hz, 2H), 7.78 (d, $J = 15.3$ Hz, 1H), 8.02 (d, $J = 9.0$ Hz, 2H). EI-MS: m/z 401 (M^+).

1-(4-(2-Hydroxyethoxy)phenyl)ethanone (8a). The reaction described above to prepare **6a** was used, and 1.79 g of **8a** was obtained in a yield of 99.4% from 4-hydroxyacetophenone and ethylene chlorohydrin. ^{1}H NMR ($CDCl_3$) δ: 2.75 (s, 3H), 4.20 (s, 2H), 4.35 (t, $J = 5.1$ Hz, 2H), 7.15 (d, $J = 9.0$ Hz, 2H), 8.13 (d, $J = 9.0$ Hz, 2H).

1-(4-(2-(2-Hydroxyethoxy)ethoxy)phenyl)ethanone (8b). The reaction described above to prepare **6b** was used, and **8b** was obtained from 4-hydroxyacetophenone and ethylene glycol mono-2-chloroethyl ether. ^{1}H NMR ($CDCl_3$) δ: 2.56 (s, 3H), 3.68 (t, $J = 4.8$ Hz 2H), 3.75−3.79 (m, 2H) 3.90 (t, $J = 5.1$ Hz, 2H), 4.21 (t, $J = 4.8$ Hz, 2H), 6.96 (d, $J = 8.7$ Hz, 2H), 7.94 (d, $J = 8.7$ Hz, 2H).

1-(4-(2-(2-(2-Hydroxyethoxy)ethoxy)ethoxy)phenyl)ethanone (8c). The reaction described above to prepare **6a** was used, and **8c** was obtained from 4-hydroxyacetophenone and 2-[2-(chloroethoxy)ethoxy]ethanol. ^{1}H NMR ($CDCl_3$) δ: 2.50 (s, 3H), 3.72−3.83 (m, 6H), 3.92 (t, $J = 4.5$ Hz, 2H), 4.22 (t, $J = 5.1$ Hz, 2H), 4.49 (t, $J = 4.2$ Hz, 1H), 4.61 (t, $J = 4.2$ Hz, 1H), 6.86 (d, $J = 8.7$ Hz, 2H), 7.80 (d, $J = 8.7$ Hz, 2H).

1-(4-(2-Fluoroethoxy)phenyl)ethanone (9a). The reaction described above to prepare **7a** was used, and 1.02 g of **9a** was obtained

in a yield of 63.3% from **8a** and DAST. ^{1}H NMR ($CDCl_3$) δ: 4.24 (d, t, J_1 = 28.2 Hz, J_2 = 4.2 Hz, 2H), 4.75 (d, t, J_1 = 47.1 Hz, J_2 = 3.9 Hz, 2H), 6.92 (d, J = 9.0 Hz, 2H), 7.89 (d, J = 9.3 Hz, 2H).

1-(4-(2-(2-Fluoroethoxy)ethoxy)phenyl)ethanone (9b). The reaction described above to prepare **7b** was used, and **9b** was obtained from **9a** and DAST. ^{1}H NMR ($CDCl_3$) δ: 2.56 (s, 3H), 3.78 (t, J = 3.3 Hz, 1H), 3.86–3.94 (m, 3H), 4.22 (t, J = 5.1 Hz, 2H), 4.51 (t, J = 3.0 Hz, 1H), 4.67 (t, J = 3.0.Hz, 1H), 6.96 (d, J = 8.7 Hz, 2H), 7.93 (d, J = 8.7 Hz, 2H). EI-MS: m/z 226 (M^+).

1-(4-(2-(2-(2-Fluoroethoxy)ethoxy)ethoxy)phenyl)ethanone (9c). The reaction described above to prepare **7c** was used, and 543 mg of **9c** was obtained from **8c** and DAST. ^{1}H NMR ($CDCl_3$) δ: 2.56 (s, 3H), 3.69–3.81 (m, 6H), 3.90 (t, J = 4.5 Hz, 2H), 4.21 (t, J = 5.1 Hz, 2H), 4.49 (t, J = 4.2 Hz, 1H), 4.65 (t, J = 4.2 Hz, 1H), 6.95 (d, J = 9.3 Hz, 2H), 7.92 (d, J = 9.0 Hz, 2H). EI-MS: m/z 270 (M^+).

(*E*)-1-(4-(2-Fluoroethoxy)phenyl)-3-(4-nitrophenyl)-2-propen-1-one (10a). The reaction described above to prepare **5** was used, and 856 mg of **10a** was obtained in a yield of 56.6% from **9a** and 4-nitrobenzaldehyde. ^{1}H NMR ($CDCl_3$) δ: 4.32 (d, t, J_1 = 27.6 Hz, J_2 = 4.2 Hz, 2H), 4.81 (d, t, J_1 = 47.4 Hz, J_2 = 4.2 Hz, 2H), 7.04 (d, J = 8.7 Hz, 2H), 7.65 (d, J = 15.6 Hz, 1H), 7.79 (d, J = 8.7 Hz, 2H), 7.82 (d, J = 12.6 Hz, 1H), 8.06 (d, J = 9.0 Hz, 2H), 8.28 (d, J = 8.7 Hz, 2H).

(*E*)-1-(4-(2-(Fluoroethoxy)ethoxy)phenyl)-3-(4-nitrophenyl)-2-propen-1-one (10b). The reaction described above to prepare **5** was used, and 128 mg of **10b** was obtained from **9b** and 4-nitrobenzaldehyde. ^{1}H NMR ($CDCl_3$) δ: 3.79 (t, J = 4.2 Hz, 1H), 3.88–4.27 (m, 3H), 4.8 (t, J = 4.8 Hz, 2H), 4.53 (t, J = 4.2 Hz, 1H), 4.69 (t, J = 4.2 Hz, 1H), 7.03 (d, J = 8.7 Hz, 2H), 7.66 (d, J = 15.6 Hz, 1H), 7.79 (d, J = 9.0 Hz, 2H), 7.81 (d, J = 15.6 Hz, 1H), 8.05 (d, J = 8.7 Hz, 2H), 8.28 (d, J = 9.0 Hz, 2H).

(*E*)-1-(4-(2-((Fluoroethoxy)ethoxy)ethoxy)phenyl)-3-(4-nitrophenyl)-2-propen-1-one (10c). The reaction described above to prepare **5** was used, and 649 mg of **10c** was obtained from **9c**. ^{1}H NMR ($CDCl_3$) δ: 3.71–3.82 (m, 6H), 3.92 (t, J = 4.5 Hz, 2H), 4.24 (t, J = 4.8 Hz, 2H), 4.50 (t, J = 4.2 Hz, 1H), 4.66 (t, J = 4.5 Hz, 1H), 7.03 (d, J = 9.3 Hz, 2H), 7.66 (d, J = 15.6 Hz, 1H), 7.79 (d, J = 9.0 Hz, 2H), 7.81 (d, J = 15.6 Hz, 1H), 8.05 (d, J = 9.3 Hz, 2H), 8.28 (d, J = 8.7 Hz, 2H).

(*E*)-3-(4-Aminophenyl)-1-(4-(2-fluoroethoxy)phenyl)-2-propen-1-one (11a). A mixture of **10a** (856 mg, 2.7 mmol), $SnCl_2$ (2.55 g, 13.5 mmol), and EtOH (10 mL) was stirred at 100 °C for 2 h. After the mixture had cooled to room temperature, 1 M NaOH (10 mL) was added. The mixture was then extracted with ethyl acetate (10 mL). The organic phase was dried over Na_2SO_4 and filtered. The solvent was removed, and the residue was purified by silica gel chromatography using chloroform as a mobile phase to give 333 mg of **11a** (43.0%). ^{1}H NMR ($CDCl_3$) δ: 4.02 (s, broad, 2H), 4.30 (d, t, J_1 = 27.6 Hz, J_2 = 4.2 Hz, 2H), 4.79 (d, t, J_1 = 47.4 Hz, J_2 = 4.2 Hz, 2H), 6.68 (d, J = 8.7 Hz, 2H), 7.00 (d, J = 8.7 Hz, 2H), 7.36 (d, J = 15.3 Hz, 1H), 7.48 (d, J = 8.4 Hz, 2H), 7.75 (d, J = 15.3 Hz, 1H), 8.03 (d, J = 6.9 Hz, 2H). EI-MS: m/z 285 (M^+).

(*E*)-3-(4-Aminophenyl)-1-(4-(2-(fluoroethoxy)ethoxy)phenyl)-2-propen-1-one (11b). The reaction described above to prepare **11a** was used, and 85 mg of **11b** was obtained from **10b**. ^{1}H NMR ($CDCl_3$) δ: 3.77–3.94 (m, 4H), 4.00 (s, broad, 2H), 4.23 (t, J = 4.5 Hz, 2H), 4.53 (t, J = 4.2 Hz, 1H), 4.69 (t, J = 4.2 Hz, 1H), 6.68 (d, J = 8.4 Hz, 2H), 6.99 (d, J = 8.7 Hz, 2H), 7.74 (d, J = 15.6 Hz, 1H), 7.48 (d, J = 8.4 Hz, 1H), 7.36 (d, J = 15.3 Hz, 1H), 8.01 (d, J = 9.0 Hz, 2H). EI-MS: m/z 329 (M^+).

(*E*)-3-(4-Aminophenyl)-1-(4-(2-((fluoroethoxy)ethoxy)ethoxy)-phenyl)-2-propen-1-one (11c). The reaction described above to prepare **11a** was used, and 206 mg of **11c** was obtained from **10c**. ^{1}H NMR ($CDCl_3$) δ: 3.70–3.83 (m, 6H), 3.89 (t, J = 4.5 Hz, 2H), 4.12 (s, broad, 2H), 4.21 (t, J = 4.8 Hz, 2H), 4.49 (t, J = 4.0 Hz, 1H), 4.65 (t, J = 3.9 Hz, 1H), 6.67 (d, J = 8.7 Hz, 2H), 6.98 (d, J = 8.7 Hz, 2H), 7.36 (d, J = 15.3 Hz, 1H), 7.47 (d, J = 8.4 Hz, 2H), 7.74 (d, J = 15.9 Hz, 1H), 8.01 (d, J = 9.0 Hz, 2H). EI-MS: m/z 373 (M^+).

(*E*)-1-(4-(2-Fluoroethoxy)phenyl)-3-(4-(methylamino)phenyl)-2-propen-1-one (12a). To a solution of **11a** (290 mg, 1.02 mmol) in DMSO (6 mL) were added CH_3I (0.18 mL, 3.05 mmol) and anhydrous K_2CO_3 (691 mg, 5.08 mmol). The reaction mixture was stirred at room temperature for 3 h and poured into water. The mixture was extracted with ethyl acetate. The organic layers were combined and dried over Na_2SO_4. Evaporation of the solvent afforded a residue, which was purified by silica gel chromatography (hexane:ethyl acetate = 2:1) to give 90 mg of **12a** (29.5%). ^{1}H NMR ($CDCl_3$) δ: 2.89 (s, 3H), 4.23 (d, t, J_1 = 27.9 Hz, J_2 = 4.2 Hz, 2H), 4.79 (d, t, J_1 = 47.4 Hz, J_2 = 4.2 Hz, 2H), 6.59 (d, J = 8.7 Hz, 2H), 6.99 (d, J = 9.0 Hz, 2H), 7.34 (d, J = 15.3 Hz, 1H), 7.51 (d, J = 8.4 Hz, 2H), 7.78 (d, J = 15.3 Hz, 1H), 8.02 (d, J = 9.3 Hz, 2H). EI-MS: m/z 299 (M^+).

(*E*)-1-(4-(2-(Fluoroethoxy)ethoxy)phenyl)-3-(4-(methylamino)-phenyl)-2-propen-1-one (12b). The reaction described above to prepare **12a** was used, and 22 mg of **12b** was obtained from **11b**. ^{1}H NMR ($CDCl_3$) δ: 2.90 (s, 3H), 3.78–3.95 (m, 4H), 3.99 (s, broad, 1H), 4.23 (t, J = 4.5 Hz, 2H), 4.53 (t, J = 4.5 Hz, 2H), 4.53 (t, J = 4.2 Hz, 1H), 4.69 (t, J = 4.2 Hz, 1H), 6.60 (d, J = 8.7 Hz, 2H), 6.99 (d, J = 8.7 Hz, 2H), 7.35 (d, J = 15.3 Hz, 1H), 7.51 (d, J = 8.7 Hz, 2H), 7.77 (d, J = 15.3 Hz, 1H), 8.02 (d, J = 8.7 Hz, 2H). EI-MS: m/z 343 (M^+).

(*E*)-1-(4-(2-((Fluoroethoxy)ethoxy)ethoxy)phenyl)-3-(4-(methylamino)phenyl)-2-propen-1-one (12c). The reaction described above to prepare **12a** was used, and 53 mg of **12c** was obtained from **11c**. ^{1}H NMR ($CDCl_3$) δ: 2.89 (s, 3H), 3.69–3.83 (m, 6H), 3.90 (t, J = 4.8 Hz, 2H), 4.12 (s, broad, 1H), 4.22 (t, J = 5.1 Hz, 2H), 4.49 (t, J = 4.2 Hz, 1H), 4.65 (t, J = 4.1 Hz, 1H), 6.60 (d, J = 8.7 Hz, 2H), 6.98 (d, J = 9.0 Hz, 2H), 7.35 (d, J = 15.3 Hz, 1H), 7.51 (d, J = 8.7 Hz, 2H), 7.76 (d, J = 15.3 Hz, 1H), 8.01 (d, J = 8.7 Hz, 2H). EI-MS: m/z 387 (M^+).

(*E*)-3-(4-Dimethylaminophenyl)-1-(4-fluorophenyl)-2-propen-1-one (13). The reaction described above to prepare **5** was used, and 209 mg of **13** was obtained from 4-fluoroacetophenone and 4-dimethylbenzaldehyde. ^{1}H NMR (300 MHz, $CDCl_3$) δ: 3.03 (s, 6H), 6.68 (d, J = 8.7 Hz, 2H), 7.15 (t, J = 8.4 Hz, 2H), 7.30 (d, J = 15.3 Hz, 1H), 7.54 (d, J = 9.0 Hz, 2H), 7.78 (d, J = 15.3 Hz, 1H), 8.02–8.06 (m, 2H). EI-MS: m/z 269 (M^+).

(*E*)-1-(4-Fluorophenyl)-3-(4-nitrophenyl)-2-propen-1-one (14). The reaction described above to prepare **5** was used, and 490 mg of **14** was obtained from 4-fluoroacetophenone and 4-nitrobenzaldehyde. ^{1}H NMR (300 MHz, $CDCl_3$) δ: 7.21 (t, J = 8.7 Hz, 2H), 7.62 (d, J = 15.9 Hz, 1H), 7.80 (d, J = 8.7 Hz, 2H), 7.84 (d, J = 15.9 Hz, 1H), 8.07–8.12 (m, 2H), 8.29 (d, J = 8.7 Hz, 2H). EI-MS: m/z 271 (M^+).

(*E*)-3-(4-Aminophenyl)-1-(4-fluorophenyl)-2-propen-1-one (15). The reaction described above to prepare **11(a–c)** was used, and 150 mg of **15** was obtained from **14**. ^{1}H NMR (300 MHz, $CDCl_3$) δ: 4.07 (s, broad, 2H), 6.67 (d, J = 8.7 Hz, 2H), 7.15 (t, J = 8.7 Hz, 2H), 7.31 (d, J = 15.6 Hz, 1H), 7.47 (d, J = 8.4 Hz, 2H), 7.75 (d, J = 15.6 Hz, 1H), 8.03 (t, J = 8.7 Hz, 2H). EI-MS: m/z 241 (M^+).

(*E*)-1-(4-Fluorophenyl)-3-(4-methylaminophenyl)-2-propen-1-one (16). The reaction described above to prepare **12(a–c)** was used, and 14 mg of **16** was obtained from **15**. ^{1}H NMR (300 MHz, $CDCl_3$) δ: 2.90 (s, 3H), 4.20 (s, broad, 1H), 6.60 (d, J = 8.7 Hz, 2H), 7.17 (d, J = 8.7 Hz, 2H), 7.30 (d, J = 15.6 Hz, 1H), 7.50 (d, J = 8.7 Hz, 2H), 7.78 (d, J = 15.6 Hz, 1H), 8.04 (d, J = 8.7 Hz, 2H). EI-MS: m/z 255 (M^+).

(*E*)-2-(2-(2-(4-(3-(4-(Dimethylamino)phenyl)acryloyl)phenoxy)-ethoxy)ethoxy)ethyl 4-methylbenzenesulfonate (17). To a solution of **6c** (108 mg, 0.27 mmol) in pyridine (3 mL) was added tosyl chloride (343.8 mg, 0.621 mmol). The reaction mixture was stirred for 3 h at room temperature. After water was added, the mixture was extracted with ethyl acetate. The organic layer was dried over Na_2SO_4, and evaporation of the solvent afforded a residue, which was purified by preparative TLC (hexane:ethyl acetate = 1:1) to give 44 mg of **17** (29.4%). ^{1}H NMR (300 MHz, $CDCl_3$) δ: 2.43 (s, 3H), 3.04 (s, 6H), 3.62–3.72 (m, 6H),

3.85−3.87 (m, 2H), 4.15−4.18 (m, 4H), 6.70 (d, J = 8.7 Hz, 2H), 6.98 (d, J = 9.0 Hz, 2H), 7.31−7.35 (m, 2H), 7.37 (d, J = 9.0 Hz, 1H), 7.55 (d, J = 8.7 Hz, 2H), 7.80 (t, J = 8.7 Hz, 3H), 8.02 (d, J = 9.0 Hz, 2H). EI-MS m/z 553 (M^+)

Radiolabeling. Procedure for Labeling of 7a, 7b, 7c, and 13 with ^{11}C. ^{11}C was produced via a ^{14}N(p,α)^{11}C reaction with 16 MeV protons on a target of nitrogen gas with an ultracompact cyclotron (CYPRIS model 325R; Sumitomo Heavy Industry Ltd.) The $^{11}CO_2$ produced was transported to an automated system for the synthesis of ^{11}C-methyl iodide (CUPID C-100; Sumitomo Heavy Industry Ltd.) and converted sequentially to [^{11}C]MeOTf by the previously described method of Jewett.[33] [^{11}C]Chalcones were produced by reacting [^{11}C]MeOTf with the normethyl precursor, **7a**, **7b**, **7c**, and **13**, (0.5 mg) in 500 μL of methyl ethyl ketone (MEK). After the complete transfer of [^{11}C]MeOTf, ^{11}C-methylation was carried out for 5 min and the reaction solvent was then dried with a stream of nitrogen gas. The residue taken up in 200 μL of acetonitrile was purified by a reverse phase HPLC system (a Shimadzu LC-6A isocratic pump, a Shimadzu SPD-6A UV detector, and a Aloka NDW-351D scintillation detector) on a Cosmosil C_{18} column (Nakalai Tesque, 5C_{18}-AR-II, 10 mm × 250 mm) with an isocratic solvent of acetonitrile/water (55/45) at a flow rate of 6.0 mL/min. The desired fraction was collected in a flask and evaporated dry. The radiochemical yield, purity, and specific activity of [^{11}C]chalcones were further confirmed by analytical reverse phase HPLC on a 5C_{18}-AR-300 column (Nakalai Tesque, 4.6 mm × 150 mm, acetonitrile/water (60/40), 1.0 mL/min).

Procedure for Labeling 7c with ^{18}F. [^{18}F]Fluoride was produced by the JSW typeBC3015 cyclotron via an ^{18}O(p,n)^{18}F reaction and passed through a Sep-Pak Light QMA cartridge (Waters) as an aqueous solution in ^{18}O-enriched water. The cartridge was dried by airflow, and the ^{18}F activity was eluted with 0.5 mL of a Kryptofix 222/K_2CO_3 solution (11 mg of Kryptofix 222 and 2.6 mg of K_2CO_3 in acetonitrile/water (86/14)). The solvent was removed at 120 °C under a stream of argon gas. The residue was azeotropically dried with 1 mL of anhydrous acetonitrile twice at 120 °C under a stream of nitrogen gas and dissolved in DMSO (1 mL). A solution of tosylate precursor **17** (1.0 mg) in DMSO (1 mL) was added to the reaction vessel containing the ^{18}F activity in DMSO. The mixture was heated at 160 °C for 5 min. Water (5 mL) was added, and the mixture was passed through a preconditioned Oasis HLB cartridge (3 cm^3) (Waters). The cartridge was washed with 10 mL of water, and the labeled compound was eluted with 2 mL of acetonitrile. The eluted compound was purified by preparative HPLC [YMC-Pack Pro C_{18} column (20 mm × 150 mm), acetonitrile/water (75/25), flow rate 9.0 mL/min]. The retention time of the major byproduct of hydrolysis (t_R = 2.7 min) was well-resolved from the desired ^{18}F-labeled product (t_R = 10.7 min). The radiochemical purity and specific activity were determined by analytical HPLC [YMC-Pack Pro C_{18} column (4.6 mm × 150 mm), acetonitrile/water (60/40), flow rate 1.0 mL/min], and [^{18}F]**7c** was obtained in a radiochemical purity of >99% with the specific activity of 35 GBq/mmol. Specific activity was estimated by comparing the UV peak intensity of the purified ^{18}F-labeled compound with a reference nonradioactive compound of known concentration.

Binding Assays Using the Aggregated Aβ peptides in Solution. Aβ(1−42) was purchased from Peptide Institute (Osaka, Japan). Aggregation was carried out by gently dissolving the peptide (0.25 mg/mL) in a buffer solution (pH 7.4) containing 10 mM sodium phosphate and 1 mM EDTA. The solution was incubated at 37 °C for 42 h with gentle and constant shaking. Binding experiments were carried out as described previously.[18] [^{125}I]DMIC with 2200 Ci/mmol of specific activity and radiochemical purity greater than 95% was prepared using the standard iododestannylation reaction. A mixture containing 50 μL of test compound (0.2 pM-400 μM in 10% EtOH), 50 μL of 0.02 nM [^{125}I]DMIC, 50 μL of Aβ(1−42) aggregates, and 850 μL of 10% EtOH was incubated at room temperature for 3 h. The mixture was then filtered through Whatman GF/B filters using a Brandel M-24 cell harvester, and the radioactivity of the filters containing the bound ^{125}I ligand was measured in a γ counter. Values for the half-maximal inhibitory concentration (IC_{50}) were determined from displacement curves of three independent experiments using GraphPad Prism 4.0, and those for the inhibition constant (K_i) were calculated using the Cheng−Prusoff equation: $K_i = IC_{50}/(1 + [L]/K_d)$, where [L] is the concentration of [^{125}I]DMIC used in the assay and K_d is the dissociation constant of DMIC (4.2 nM).[19] DMIC and IMPY used as test compounds for the inhibition assay were synthesized as reported previously.[19,34]

Biodistribution in Normal Mice. Experiments with animals were conducted in accordance with our institutional guidelines and approved by the Nagasaki University Animal Care Committee and the Kyoto University Animal Care Committee. A 100 μL amount of a saline solution containing the radiolabeled agent (3.7 MBq), EtOH (10%), and ascorbic acid (1 mg/mL) was injected directly into the tail vein of ddY mice (5-week-old, 22−25 g). Groups of five mice were sacrificed at various post-injection time points. The organs of interest were removed and weighed, and the radioactivity was measured with an automatic γ counter (COBRAII, Packard).

Staining of Aβ Plaques in Brain Sections of Tg2576 Transgenic Mice. The Tg2576 transgenic mice (female, 20-month-old) and wild-type (female, 20-month-old) mice were used as an Alzheimer's model and an age-matched control, respectively. After the mice were sacrificed by decapitation, the brains were immediately removed and frozen in powdered dry ice. The frozen blocks were sliced into serial sections 10 μm thick. Each slide was incubated with a 50% EtOH solution (100 μM) of compound **7c** for 10 min. The sections were washed with 50% EtOH for 3 min two times. After drying, the sections were then examined using a microscope (Nikon, Eclipse 80i) equipped with a B-2A filter set (excitation, 450−490 nm; diachronic mirror, 505 nm; long-pass filter, 520 nm). Thereafter, the serial sections were also immunostained with 3,3′-diaminobenzidine (DAB) as a chromogen using monoclonal antibodies against Aβ (amyloid β-protein immunohistostain kit, WAKO).

In Vitro Autoradiography Using Human AD Brains. Postmortem brain tissues from an autopsy-confirmed case of AD (73-year-old male) were obtained from BioChain Institute Inc. The presence and localization of plaques on the sections were confirmed with immunohistochemical staining using a monoclonal Aβ antibody as described above. The sections were incubated with [^{18}F]**7c** (54 μCi/200 μL) for 1 h at room temperature. They were then washed in 50% EtOH (two 1 min wash), before being rinsed with water for 30 s. After drying, the ^{18}F-labeled sections were exposed to a BAS imaging plate (Fuji Film, Tokyo, Japan) for 6 h. Ex vivo autoradiographic images were obtained using a BAS5000 scanner system (Fuji Film). After autoradiographic examination, the same sections were stained by thioflavin-S to confirm the presence of Aβ plaques. For the staining of thioflavin-S, sections were immersed in a 0.125% thioflavin-S solution containing 50% EtOH for 3 min and washed in 50% EtOH. After drying, the sections were then examined using a microscope (Nikon, Eclipse 80i) equipped with a B-2A filter set (excitation, 450−490 nm; diachronic mirror, 505 nm; long-pass filter, 520 nm).

Acknowledgment. This study was supported by the Program for Promotion of Fundamental Studies in Health Sciences of the National Institute of Biomedical Innovation (NIBIO), a Health Labour Sciences Research Grant, and a Grant-in-Aid for Young Scientists (A) and Exploratory Research from the Ministry of Education, Culture, Sports, Science and Technology, Japan.

Supporting Information Available: Representative HPLC chromatograms of [^{18}F]**7c**. This material is available free of charge via the Internet at http://pubs.acs.org.

References

(1) Hardy, J. A.; Higgins, G. A. Alzheimer's disease: the amyloid cascade hypothesis. *Science* **1992**, *256*, 184–185.

(2) Selkoe, D. J. Alzheimer's disease: genes, proteins, and therapy. *Physiol. Rev.* **2001**, *81*, 741–766.

(3) Nordberg, A. PET imaging of amyloid in Alzheimer's disease. *Lancet Neurol.* **2004**, *3*, 519–527.

(4) Mathis, C. A.; Wang, Y.; Klunk, W. E. Imaging β-amyloid plaques and neurofibrillary tangles in the aging human brain. *Curr. Pharm. Des.* **2004**, *10*, 1469–1492.

(5) Klunk, W. E.; Engler, H.; Nordberg, A.; Wang, Y.; Blomqvist, G.; Holt, D. P.; Bergstrom, M.; Savitcheva, I.; Huang, G. F.; Estrada, S.; Ausen, B.; Debnath, M. L.; Barletta, J.; Price, J. C.; Sandell, J.; Lopresti, B. J.; Wall, A.; Koivisto, P.; Antoni, G.; Mathis, C. A.; Langstrom, B. Imaging brain amyloid in Alzheimer's disease with Pittsburgh Compound-B. *Ann. Neurol.* **2004**, *55*, 306–319.

(6) Mathis, C. A.; Wang, Y.; Holt, D. P.; Huang, G. F.; Debnath, M. L.; Klunk, W. E. Synthesis and evaluation of ^{11}C-labeled 6-substituted 2-arylbenzothiazoles as amyloid imaging agents. *J. Med. Chem.* **2003**, *46*, 2740–2754.

(7) Verhoeff, N. P.; Wilson, A. A.; Takeshita, S.; Trop, L.; Hussey, D.; Singh, K.; Kung, H. F.; Kung, M. P.; Houle, S. In vivo imaging of Alzheimer disease β-amyloid with [^{11}C]SB-13 PET. *Am. J. Geriatr. Psychiatry* **2004**, *12*, 584–595.

(8) Ono, M.; Wilson, A.; Nobrega, J.; Westaway, D.; Verhoeff, P.; Zhuang, Z. P.; Kung, M. P.; Kung, H. F. ^{11}C-Labeled stilbene derivatives as Abeta-aggregate-specific PET imaging agents for Alzheimer's disease. *Nucl. Med. Biol.* **2003**, *30*, 565–571.

(9) Small, G. W.; Kepe, V.; Ercoli, L. M.; Siddarth, P.; Bookheimer, S. Y.; Miller, K. J.; Lavretsky, H.; Burggren, A. C.; Cole, G. M.; Vinters, H. V.; Thompson, P. M.; Huang, S. C.; Satyamurthy, N.; Phelps, M. E.; Barrio, J. R. PET of brain amyloid and tau in mild cognitive impairment. *N. Engl. J. Med.* **2006**, *355*, 2652–2663.

(10) Shoghi-Jadid, K.; Small, G. W.; Agdeppa, E. D.; Kepe, V.; Ercoli, L. M.; Siddarth, P.; Read, S.; Satyamurthy, N.; Petric, A.; Huang, S. C.; Barrio, J. R. Localization of neurofibrillary tangles and β-amyloid plaques in the brains of living patients with Alzheimer disease. *Am. J. Geriatr. Psychiatry* **2002**, *10*, 24–35.

(11) Rowe, C. C.; Ackerman, U.; Browne, W.; Mulligan, R.; Pike, K. L.; O'Keefe, G.; Tochon-Danguy, H.; Chan, G.; Berlangieri, S. U.; Jones, G.; Dickinson-Rowe, K. L.; Kung, H. P.; Zhang, W.; Kung, M. P.; Skovronsky, D.; Dyrks, T.; Holl, G.; Krause, S.; Friebe, M.; Lehman, L.; Lindemann, S.; Dinkelborg, L. M.; Masters, C. L.; Villemagne, V. L. Imaging of amyloid β in Alzheimer's disease with ^{18}F-BAY94-9172, a novel PET tracer: proof of mechanism. *Lancet Neurol.* **2008**, *7*, 129–135.

(12) Zhang, W.; Oya, S.; Kung, M. P.; Hou, C.; Maier, D. L.; Kung, H. F. F-18 polyethyleneglycol stilbenes as PET imaging agents targeting Aβ aggregates in the brain. *Nucl. Med. Biol.* **2005**, *32*, 799–809.

(13) Lockhart, A. Imaging Alzheimer's disease pathology: one target, many ligands. *Drug Discovery Today* **2006**, *11*, 1093–1099.

(14) Ye, L.; Morgenstern, J. L.; Gee, A. D.; Hong, G.; Brown, J.; Lockhart, A. Delineation of positron emission tomography imaging agent binding sites on β-amyloid peptide fibrils. *J. Biol. Chem.* **2005**, *280*, 23599–235604.

(15) Lockhart, A.; Ye, L.; Judd, D. B.; Merritt, A. T.; Lowe, P. N.; Morgenstern, J. L.; Hong, G.; Gee, A. D.; Brown, J. Evidence for the presence of three distinct binding sites for the thioflavin T class of Alzheimer's disease PET imaging agents on β-amyloid peptide fibrils. *J. Biol. Chem.* **2005**, *280*, 7677–7684.

(16) Ono, M.; Yoshida, N.; Ishibashi, K.; Haratake, M.; Arano, Y.; Mori, H.; Nakayama, M. Radioiodinated flavones for in vivo imaging of β-amyloid plaques in the brain. *J. Med. Chem.* **2005**, *48*, 7253–7260.

(17) Ono, M.; Watanabe, R.; Kawashima, H.; Kawai, T.; Watanabe, H.; Haratake, M.; Saji, H.; Nakayama, M. ^{18}F-Labeled flavones for in vivo imaging of β-amyloid plaques in Alzheimer's brains. *Bioorg. Med. Chem.* **2009**, *17*, 2069–2076.

(18) Ono, M.; Hori, M.; Haratake, M.; Tomiyama, T.; Mori, H.; Nakayama, M. Structure–activity relationship of chalcones and related derivatives as ligands for detecting of β-amyloid plaques in the brain. *Bioorg. Med. Chem.* **2007**, *15*, 6388–6396.

(19) Ono, M.; Haratake, M.; Mori, H.; Nakayama, M. Novel chalcones as probes for in vivo imaging of β-amyloid plaques in Alzheimer's brains. *Bioorg. Med. Chem.* **2007**, *15*, 6802–6809.

(20) Maya, Y.; Ono, M.; Watanabe, H.; Haratake, M.; Saji, H.; Nakayama, M. Novel radioiodinated aurones as probes for SPECT imaging of β-amyloid plaques in the brain. *Bioconjugate Chem.* **2009**, *20*, 95–101.

(21) Ono, M.; Maya, Y.; Haratake, M.; Ito, K.; Mori, H.; Nakayama, M. Aurones serve as probes of β-amyloid plaques in Alzheimer's disease. *Biochem. Biophys. Res. Commun.* **2007**, *361*, 116–121.

(22) Stephenson, K. A.; Chandra, R.; Zhuang, Z. P.; Hou, C.; Oya, S.; Kung, M. P.; Kung, H. F. Fluoro-pegylated (FPEG) imaging agents targeting Aβ aggregates. *Bioconjugate Chem.* **2007**, *18*, 238–246.

(23) Qu, W.; Kung, M. P.; Hou, C.; Oya, S.; Kung, H. F. Quick assembly of 1,4-diphenyltriazoles as probes targeting β-amyloid aggregates in Alzheimer's disease. *J. Med. Chem.* **2007**, *50*, 3380–3387.

(24) Zhang, W.; Oya, S.; Kung, M. P.; Hou, C.; Maier, D. L.; Kung, H. F. F-18 stilbenes as PET imaging agents for detecting β-amyloid plaques in the brain. *J. Med. Chem.* **2005**, *48*, 5980–5988.

(25) Kung, M. P.; Hou, C.; Zhuang, Z. P.; Zhang, B.; Skovronsky, D.; Trojanowski, J. Q.; Lee, V. M.; Kung, H. F. IMPY: an improved thioflavin-T derivative for in vivo labeling of β-amyloid plaques. *Brain Res.* **2002**, *956*, 202–210.

(26) Hsiao, K.; Chapman, P.; Nilsen, S.; Eckman, C.; Harigaya, Y.; Younkin, S.; Yang, F.; Cole, G. Correlative memory deficits, Aβ elevation, and amyloid plaques in transgenic mice. *Science* **1996**, *274*, 99–102.

(27) Kuntner, C.; Kesner, A. L.; Bauer, M.; Kremslehner, R.; Wanek, T.; Mandler, M.; Karch, R.; Stanek, J.; Wolf, T.; Muller, M.; Langer, O. Limitations of small animal PET imaging with [^{18}F]FDDNP and FDG for quantitative studies in a transgenic mouse model of Alzheimer's disease. *Mol. Imaging Biol.* **2009**, *11*, 236–240.

(28) Klunk, W. E.; Lopresti, B. J.; Ikonomovic, M. D.; Lefterov, I. M.; Koldamova, R. P.; Abrahamson, E. E.; Debnath, M. L.; Holt, D. P.; Huang, G. F.; Shao, L.; DeKosky, S. T.; Price, J. C.; Mathis, C. A. Binding of the positron emission tomography tracer Pittsburgh compound-B reflects the amount of amyloid-β in Alzheimer's disease brain but not in transgenic mouse brain. *J. Neurosci.* **2005**, *25*, 10598–10606.

(29) Maeda, J.; Ji, B.; Irie, T.; Tomiyama, T.; Maruyama, M.; Okauchi, T.; Staufenbiel, M.; Iwata, N.; Ono, M.; Saido, T. C.; Suzuki, K.; Mori, H.; Higuchi, M.; Suhara, T. Longitudinal, quantitative assessment of amyloid, neuroinflammation, and anti-amyloid treatment in a living mouse model of Alzheimer's disease enabled by positron emission tomography. *J. Neurosci.* **2007**, *27*, 10957–10968.

(30) Toyama, H.; Ye, D.; Ichise, M.; Liow, J. S.; Cai, L.; Jacobowitz, D.; Musachio, J. L.; Hong, J.; Crescenzo, M.; Tipre, D.; Lu, J. Q.; Zoghbi, S.; Vines, D. C.; Seidel, J.; Katada, K.; Green, M. V.; Pike, V. W.; Cohen, R. M.; Innis, R. B. PET imaging of brain with the β-amyloid probe, [^{11}C]6-OH-BTA-1, in a transgenic mouse model of Alzheimer's disease. *Eur. J. Nucl. Med. Mol. Imaging* **2005**, *32*, 593–600.

(31) Skovronsky, D. M.; Zhang, B.; Kung, M. P.; Kung, H. F.; Trojanowski, J. Q.; Lee, V. M. In vivo detection of amyloid plaques in a mouse model of Alzheimer's disease. *Proc. Natl. Acad. Sci. U.S.A* **2000**, *97*, 7609–7614.

(32) Saido, T. C.; Iwatsubo, T.; Mann, D. M.; Shimada, H.; Ihara, Y.; Kawashima, S. Dominant and differential deposition of distinct β-amyloid peptide species, A β N3(pE), in senile plaques. *Neuron* **1995**, *14*, 457–466.

(33) Jewett, D. M. A simple synthesis of [^{11}C]methyl triflate. *Int. J. Radiat. Appl. Instrum. A* **1992**, *43*, 1383–1385.

(34) Zhuang, Z. P.; Kung, M. P.; Wilson, A.; Lee, C. W.; Plossl, K.; Hou, C.; Holtzman, D. M.; Kung, H. F. Structure–activity relationship of imidazo[1,2-*a*]pyridines as ligands for detecting β-amyloid plaques in the brain. *J. Med. Chem.* **2003**, *46*, 237–243.

Bioorganic & Medicinal Chemistry 17 (2009) 7002–7007

Contents lists available at ScienceDirect

Bioorganic & Medicinal Chemistry

journal homepage: www.elsevier.com/locate/bmc

Push–pull benzothiazole derivatives as probes for detecting β-amyloid plaques in Alzheimer's brains

Masahiro Ono [a,*,†], Shun Hayashi [a,†], Hiroyuki Kimura [a], Hidekazu Kawashima [b], Morio Nakayama [c], Hideo Saji [a,*]

[a] Graduate School of Pharmaceutical Sciences, Kyoto University, 46-29 Yoshida Shimoadachi-cho, Sakyo-ku, Kyoto 606-8501, Japan
[b] Graduate School of Medicine, Kyoto University, Shogoin Kawahara-cho, Kyoto 606-8507, Japan
[c] Graduate School of Biomedical Sciences, Nagasaki University, 1-14 Bunkyo-machi, Nagasaki 852-8521, Japan

ARTICLE INFO

Article history:
Received 29 June 2009
Revised 4 August 2009
Accepted 4 August 2009
Available online 20 August 2009

Keywords:
β-Amyloid
Push–pull dye
Imaging
Alzheimer's disease

ABSTRACT

We synthesized push–pull benzothiazole derivatives and evaluated their potential as β-amyloid imaging probes. In binding experiments in vitro, the benzothiazoles showed excellent affinity for synthetic Aβ(1-42) aggregates. β-Amyloid plaques in the mouse and human brain were clearly visualized with the benzothiazoles, reflecting the results in vitro. These compounds may be a useful scaffold for the development of novel PET/SPECT and fluorescent tracers for detecting β-amyloid in Alzheimer's brains.

1. Introduction

The formation of β-amyloid (Aβ) plaques is a key neurodegenerative event in Alzheimer's disease (AD).[1,2] Since the imaging of these plaques in vivo may lead to the presymptomatic diagnosis of AD, many molecular probes for this purpose, including PET/SPECT and MRI tracers, have been developed.[3–12] The PET ligand [^{11}C]-2-(4-(methylamino)phenyl)-6-hydroxybenzothiazole (6-OH-BTA-1 or PIB) with a benzothiazole backbone (Fig. 1) has shown particular promise in early clinical trials and is currently being used in a number of human studies.[13–15] In addition to PET/SPECT and MRI probes, much attention has focused on the development of near-infrared fluorescent (NIRF) probes targeting Aβ plaques.[16–18] NIRF probes are typically small molecule fluorescent dyes designed to absorb and emit light in the near-infrared region, where tissue scattering and absorption is lowest. The simple synthesis, low-cost, and long shelf-life of NIRF probes, together with the low-cost of optical imaging devices, present an attractive alternative to MRI and PET/SPECT techniques.

Among NIRF probes reported, to date, NIAD crosses the blood–brain barrier, selectively binds Aβ with high affinity, clears quickly from the brain, and absorbs and emits within the near-infrared region (650–900 nm), often called the 'optical window' (Fig. 1).[17] A series of NIAD derivatives have been designed and synthesized based on a classical push–pull architecture with terminal donor (hydroxy or dimethylamino group) and acceptor (dicyanomethylene group) moieties that are interconnected by a highly polarized bridge (dithienylethenyl group), because various donor and acceptor groups can be used to manipulate the relative energies of HOMO and LUMO and obtain the desired long wavelength of absorption/emission bands.[17]

On the basis of this approach to the molecular design, we planned to develop novel push–pull dyes for detecting Aβ plaques in the brain. We selected benzothiazole or styrylbenzothiazole as the highly polarized bridge, a dimethylamino group as the donor, and a dicyanomethylene group as the acceptor. In the present study, we designed and synthesized two benzothiazole-derived push–pull dyes (PP-BTA-1 and PP-BTA-2 in Fig. 2), and evaluated their biological potential as probes for detecting Aβ plaques in the brain. To our knowledge, this is the first time push–pull benzothiazole derivatives have been proposed as Aβ imaging probes for detecting AD.

2. Results and discussion

The target benzothiazole derivatives were prepared as shown in Schemes 1 and 2. PP-BTA-1 (**4**) was successfully synthesized in a yield of 21.4% according to methods reported previously (Scheme

* Corresponding authors. Tel.: +81 75 753 4608; fax: +81 75 753 4568 (M.O), tel.: +81 75 753 4556; fax: +81 75 753 4568 (H.S.).
E-mail addresses: ono@pharm.kyoto-u.ac.jp (M. Ono), hsaji@pharm.kyoto-u.ac.jp (H. Saji).
† These authors contributed equally to this work.

0968-0896/$ - see front matter © 2009 Elsevier Ltd. All rights reserved.
doi:10.1016/j.bmc.2009.08.032

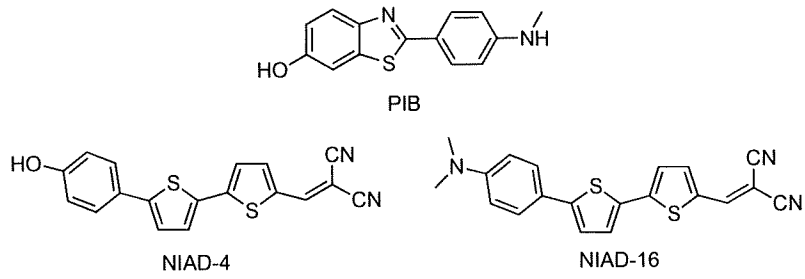

Figure 1. Chemical structures of PIB, NIAD-4 and NIAD-16.

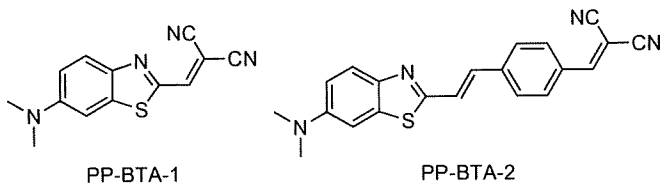

Figure 2. Chemical structures of push–pull benzothiazole derivatives reported in this paper.

1).[19] The formation of styrylbenzothiazole in the synthesis of PP-BTA-2 (**7**) (Scheme 2) was achieved by a Wadsworth–Emmons reaction between diethyl (4-cyanobenzyl)phosphonate and 6-dimethylaminobenzothiazole-2-carbaldehyde. The desired (*E*)-styrylbenzothiazole derivative was prepared in a yield of 23.0%. The cyano group was converted to a formyl group by a reaction with DIBAL-H as reported.[20] The target PP-BTA-2 was prepared by the condensation of carbaldehyde with malononitrile.

NIRF imaging in vivo requires the development of new fluorescent compounds with optimal fluorescent properties and high affinity for Aβ plaques. First, we evaluated the fluorescent properties (absorption/emission wavelengths) of PP-BTA-1 and PP-BTA-2. PP-BTA-1 and PP-BTA-2 exhibited absorption/emission peaks at 540/634 nm and 410/529 nm in EtOH, respectively. The extension of π-conjugation generally leads to absorption/emission bands with longer wavelengths. However, PP-BTA-2 showed a shorter wavelength than PP-BTA-1 despite a longer π-conjugation. On the other hand, because the wavelength of PP-BTA-1 is close to the near-infrared region, a slight modification should lead to a wavelength appropriate for imaging in vivo. Furthermore, when PP-BTA-1 and PP-BTA-2 existed in a solution containing Aβ(1-42) aggregates, the fluorescence intensity of PP-BTA-1 and PP-BTA-2 increased with the concentration of Aβ(1-42) aggregates, indicating affinity for Aβ aggregates (Fig. 3).

To quantify the affinity of push–pull benzothiazole derivatives for Aβ plaques, we carried out inhibition assays on the binding to Aβ(1-42) aggregates with thioflavin T as a competing ligand. PP-BTA-1 and PP-BTA-2 displaced thioflavin T in a dose-dependent manner, indicating that they have affinity for Aβ(1-42) aggregates (Fig. 4). In addition, this result suggests that PP-BTA-1 and PP-BTA-2 may occupy a binding site on Aβ aggregates similar to that of thioflavin T. The apparent IC_{50} values for PP-BTA-1, PP-BTA-2 and PIB were 0.12, 0.11 and 0.67 μM, respectively (Table 1). The IC_{50} of

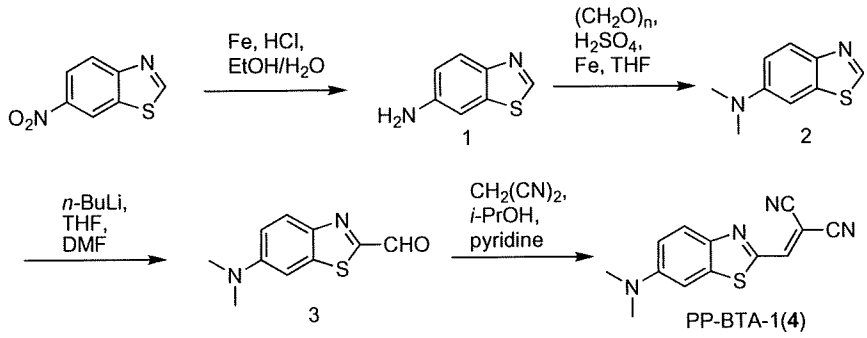

Scheme 1.

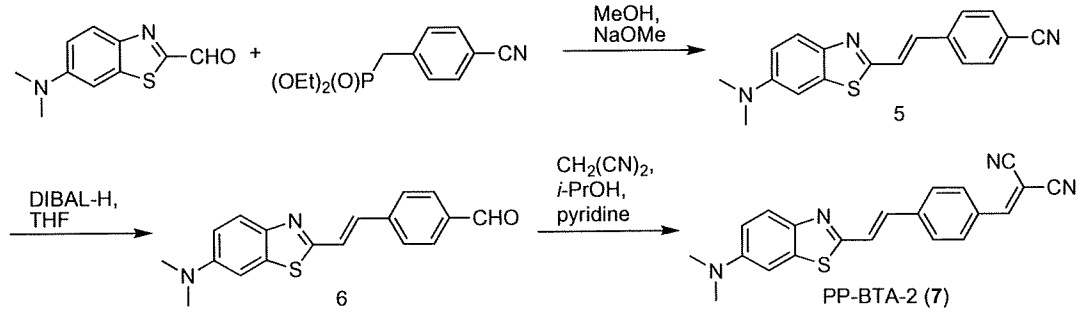

Scheme 2.